Polarization transfer coefficients from high-resolution polarized proton scattering at 0°

Polarisationstransferobservablen aus hochauflösender polarisierter Protonenstreuung unter 0°

Bachelor-Thesis by Johannes Simonis

October 2011

TECHNISCHE UNIVERSITÄT DARMSTADT

Fachbereich Physik
Institut für Kernphysik

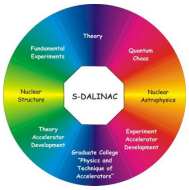

Supported by the DFG through SFB 634 and 446JAP 113/267/0-2.

Polarization transfer coefficients from high-resolution polarized proton scattering at 0°
Polarisationstransferobservablen aus hochauflösender polarisierter Protonenstreuung unter 0°

vorgelegte Bachelor-Thesis von Johannes Simonis

1. Gutachten: Prof. Dr. Peter von Neumann-Cosel
2. Gutachten: Andreas Krugmann, M. Sc.

Tag der Einreichung:

Zusammenfassung

Hochauflösende Streuexperimente mit einem polarisierten Protonenstrahl wurden am Research Center for Nuclear Physics (RCNP) in Osaka, Japan durchgeführt. Die Polarisationstransferkoeffizienten D_{SS} und D_{LL} wurden für verschiedene Kerne mit einer Protonenstrahlenergie von 295 MeV unter 0° gemessen. Diese bieten eine einsatzstarke modellunabhängige Möglichkeit den Spinflip-Charakter von Übergängen zu untersuchen. Die dominierenden Beiträge in polarisierter Protonenstreuung unter 0° stammen von E1 Anregungen durch die Coulombwechselwirkung zwischen Projektil und Target sowie von Spin-M1-Anregungen hervorgerufen durch den Spin-Isospin-Anteil der Proton-Kern-Wechselwirkung. Um die entsprechende Stärkeverteilung extrahieren zu können, müssen die E1 und Spin-M1-Beiträge getrennt werden. Am Beispiel ^{12}C wurden verschiedene Methoden zur Extraktion der Polarisationstransferobservablen untersucht und anhand von Übergängen mit bekanntem Spinflip-Charakter getestet. Darüber hinaus wurden das Anregungsspektrum und der vollständige Spintransfer Σ für die Kerne ^{208}Pb and ^{120}Sn extrahiert.

Abstract

High-resolution polarized proton scattering experiments were performed at the Research Center for Nuclear Physics (RCNP) in Osaka, Japan. Polarization transfer coefficients D_{SS} and D_{LL} have been measured for different nuclei with a proton beam energy of 295 MeV at 0°. Polarization transfer coefficients are a powerful model-independent probe to study the spinflip character of transitions in nuclei. The dominating contributions in polarized proton scattering at 0° originate from E1 excitation due to Coulomb projectile-target interaction and spin-M1 transitions caused by the spin-isospin part of the proton-nucleus interaction. In order to extract the coresponding strength distribution they have to be separated. Using the example of ^{12}C different methods for the extraction of polarization transfer observables have been studied and were tested by means of transitions with known spinflip character. Moreover, the excitation energy spectrum and the total spin transfer Σ have been determined for the nuclei ^{208}Pb and ^{120}Sn.

Contents

List of Figures

List of Tables

1 Introduction

The complete dipole strength in nuclei provides important information on different aspects of nuclear structure. Of particular interest is the strength below the giant dipole resonance (GDR), the so-called pygmy dipole resonance (PDR). The characteristics of the PDR are related to fundamental properties as the neutron skin [1] and the asymmetry energy [2]. The strength distribution of the PDR may also impact on the r-process nucleosynthesis [3]. Moreover, microscopic models are tested as they reproduce the qualitative nature of the PDR but differ in the predictions of the centroid energy and the total strength as recently demonstrated for the chain of stable tin isotopes [4]. Another topic of interest is the spinflip M1 strength where quenching is an unsolved problem [5].

One opportunity to study the E1 pygmy resonance near the particle emission threshold are nuclear resonance fluorescence (NRF) experiments [6]. NRF measurements of stable tin isotopes ^{112,120}Sn have been performed at the Superconducting DArmstadt electron Linear Accelerator S-DALINAC [7]. These experiments provide a high energy resolution but are limited to the particle emission threshold, which is about 9.1 MeV for neutron separation in ^{120}Sn. For higher endpoint energies neutrons from (γ, n) reactions would lead to a significant increase of background events. In most analyses the unknown ground-state decay branching ratio is assumed to be 100 %. This marks a lower limit of the cross section. Alternatively a correction involving a statistical model calculation estimates an upper limit of the cross section [8].

A new experimental tool for the study of the complete dipole strength distribution is high-resolution polarized proton scattering at 0°. The advantage of 0° scattering is the selectivity to excitations with low angular momentum transfer. Unpolarized and polarized proton scattering experiments at forward angles have been performed since the 1980's for example at the Tri University Meson Facility (TRIUMF) in Vancouver, Canada [9] and at the Kernfysisch Versneller Instituut (KVI) in Groningen, The Netherlands [10]. For ^{120}Sn two forward-angle inelastic proton scattering measurements have been done. An experiment with protons of 200 MeV from the TRIUMF accelerator at a scattering angle of 4° did not show indications of a resonance-like structure at small excitation energies [11], while the other one performed at the Orsay synchrocyclotron in Orsay, France with the same proton energy and at the same scattering angle identified a broad bump near 8.4 MeV. It's angular distribution was found to agree with pure $\Delta L = 0$ spinflip transitions suggesting an M1 nature [12].

However, high energy-resolution inelastic scattering experiments at 0° have been an experimental challenge. The beam exits the spectrometer very close to the focal plane detectors due to nearly the same magnetic rigidity of the scattered protons and the beam itself. Thus, the experiment is very sensitive to the beam halo. High energy resolution inelastic proton scattering at 0°

has first been successfully performed at the now decommissioned K600 magnetic spectrometer at the Indiana University Cyclotron Facility (IUCF) in Bloomington, USA. For incident energies of 160 MeV an energy resolution of 35 keV was achieved [13]. At a beam energy of 295 MeV a high energy resolution of even less than 20 keV (FWHM) for inelastic proton scattering at and close to 0° was realized at the Research Center for Nuclear Physics (RCNP) in Osaka, Japan [14]. (p, p') scattering at 0° and an incident energy of 200 MeV with an energy-resolution of 45 keV (FWHM) utilizing the faint-beam dispersion-matching technique at iThemba LABS in Somerset West, South Africa has been reported recently [15].

Inelastic proton scattering experiments at 0° for ^{120}Sn have been performed with sideway and longitudinal polarized beam in autumn of 2008 and 2009 at a beam energy of 295 MeV at the RCNP [16]. The intermediate energy region of 300 MeV provides an optimum condition for the study of spin-isospin excitations. At very forward angles, E1 excitation is due to Coulomb projectile-target interaction and spin-M1 excitation is caused by the spin-isospin part of the proton-nucleus interaction. Hence a separation of E1 and spin-M1 parts of the cross section is necessary. One approach to this goal involving the measurement of polarization transfer coeffients (PTC) D_{SS} and D_{LL} enables the separation of spinflip and non-spinflip contributions to the cross section in a model-independent way. The method of polarization transfer coefficients has been successfully applied to ^{12}C in Ref. [17] and ^{16}O in Ref. [18]. Another method is a multipole decomposition analysis (MDA) of the angular distributions. Both methods have been applied to ^{208}Pb recently and agree well within the error bars [19]. A measurement of the polarization transfer coefficients D_{SS} and D_{LL} for the heavy deformed nucleus ^{154}Sm [20] has been performed in May 2011 including a short unpolarized study of ^{144}Sm. The analysis for both nuclei is underway [21].

The aim of the present thesis is a study of polarization transfer coefficients in the nucleus ^{120}Sn as a tool for a separation of E1 and spin-M1 cross sections. In Section 2 the theory of inelastic proton scattering and polarization transfer coefficients is described. The cyclotron facility at RCNP and the experimental setup are presented in Section 3. Main analysis steps for ^{120}Sn are performed in Section 4. Two methods (sector method and estimator method) for the extraction of polarization transfer coefficients are compared for data in ^{12}C as a reference case in Section 5.1. In Section 5.2 and 5.3 the superior one (estimator method) is applied to ^{208}Pb and ^{120}Sn data. The thesis closes with a summary and an outlook.

2 Theoretical background

2.1 Inelastic proton scattering

In inelastic proton scattering the projectile-target interaction occurs via nuclear and Coulomb forces. Due to Coulomb interaction the electromagnetic excitation of electric dipole transitions is strong at extreme forward angles. Spinflip excitations caused by the strong interaction are described using an effective nucleon-nucleus interaction.

2.2 Coulomb excitation

For large impact parameters $b > r_{Coulomb}$ the nuclear excitation cross sections are small in comparison with those due to Coulomb interaction. Here, $r_{Coulomb} = r_p + r_t$ denotes the sum of the projectile and target radii, respectively. In the classical approach the projectile is considered as a point-like charge moving with negligible recoil in the repulsive Coulomb field of the target nucleus or vice versa. The hyperbolic trajectory of the projectile is shown in Fig. 2.1. The

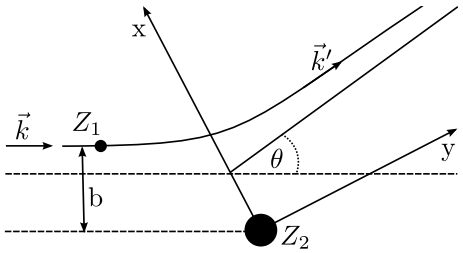

Figure 2.1: Inelastic Coulomb scattering of a projectile with momentum $\vec{k}$ and charge Z_1 off a target with charge Z_2.

momentum transfer $q = |\vec{k} - \vec{k}'|$ depending on the mass m and the velocity v_0 of the projectile and the scattering angle θ is given by

$$q = 2mv_0 \sin\left(\frac{\theta}{2}\right) . \tag{2.1}$$

The energy of the incoming beam E_p can be written as

$$E_p = mc^2 = \frac{q}{2\sin\left(\frac{\theta}{2}\right)} \frac{c^2}{v_0} . \tag{2.2}$$

With the Rutherford scattering formula

$$\left(\frac{\mathrm{d}\sigma}{\mathrm{d}\Omega}\right)_{Ruth} = \left(\frac{1}{4\pi\epsilon_0}\frac{Z_1 Z_2 e^2}{4E_p}\right)^2 \frac{1}{\sin^4\left(\frac{\theta}{2}\right)} \tag{2.3}$$

the differential cross section can be written as

$$\frac{\mathrm{d}\sigma}{\mathrm{d}\Omega} = \left(\frac{1}{4\pi\epsilon_0}\frac{Z_1 Z_2 e^2 v_0}{2qc^2}\frac{1}{\sin\left(\frac{\theta}{2}\right)}\right)^2 . \tag{2.4}$$

For small momentum transfers one concludes that cross sections due to inelastic Coulomb scattering are large. For relativistic velocities of the projectile the Mott cross section

$$\left(\frac{\mathrm{d}\sigma}{\mathrm{d}\Omega}\right)_{Mott} = \left(\frac{\mathrm{d}\sigma}{\mathrm{d}\Omega}\right)_{Ruth}\left[1-\beta^2\sin^2\left(\frac{\theta}{2}\right)\right] \tag{2.5}$$

has to be considered. Here, β denotes the relativistic Lorentz factor.
In the framework of the equivalent photon method [22], Coulomb excitation is interpreted as the absorption of virtual photons by the target nucleus. The virtual photons are produced by the moving projectile. The equivalent photon number denotes the number of real photons that would have an equivalent net effect for one particular transition. Furthermore, the equivalent photon number is linked to the Fourier transformation of the time-dependent electromagnetic field produced by the projectile. The Coulomb excitation cross section for initial (i) and final state (f) can be expressed in terms of the equivalent photon number $N_{\pi\lambda}$ and the photoabsorption cross section $\sigma_\gamma^{\pi\lambda}$ as

$$\sigma_{i\to f} = \sum_{\pi\lambda}\int N_{\pi\lambda}(E_\gamma)\sigma_\gamma^{\pi\lambda}(E_\gamma)\frac{\mathrm{d}E_\gamma}{E_\gamma} . \tag{2.6}$$

Here, π and λ denote the parity and the multipolarity of the transition and E_γ stands for the energy of the photons. Inserting the photoabsorption cross section for real photons which is given by

$$\sigma_\gamma^{\pi\lambda}(E_\gamma) = \frac{(2\pi)^3(\lambda+1)}{\lambda[(2\lambda+1)!!]^2}\sum_f \rho_f(\epsilon)k^{2\lambda-1}B(\pi\lambda) \tag{2.7}$$

leads to $\sigma_{i\to f} \simeq B(\pi\lambda)$. For electric dipole transitions one can conclude that the Coulomb excitation cross section is proportional to the E1 strength distribution. $\rho_f(\epsilon)$ represents the density of final states for the target with energy $E_f = E_i + \epsilon$ and $k = \omega/c$.

2.3 Nucleon-nucleus interaction

If the incoming proton energy is sufficiently high, the reaction can be described by the distorted wave impulse approximation (DWIA) [23] neglecting the potential energy of the target nucleons. The proton-nucleus interaction can be described as the sum of the two-particle interactions between the projectile and the individual nucleons in the nucleus. For nucleon scattering the following excitation modes are possible

- isoscalar non-spinflip ($\Delta T = 0$, $\Delta S = 0$),
- isoscalar spinflip ($\Delta T = 0$, $\Delta S = 1$),
- isovector non-spinflip ($\Delta T = 1$, $\Delta S = 0$),
- isovector spinflip ($\Delta T = 1$, $\Delta S = 1$).

The effective proton-nucleus interaction of Franey and Love [23] valid for proton energies 100−800 MeV is given by

$$V_{ip}(r_{ip}) = V^C(r_{ip}) + V^{LS}(r_{ip})\,\vec{L}\cdot\vec{S} + V^T(r_{ip})\,S_{ip}\,, \tag{2.8}$$

where i indicates the interacting nucleon within the nucleus. It considers central (V^C), spin-orbit (V^{LS}) and tensor interaction (V^T) and uses the quantities

$\vec{L}$	relative angular momentum
$\vec{S} = \vec{\sigma}_i + \vec{\sigma}_p$	relative spin
$\vec{L}\cdot\vec{S}$	spin-orbit operator
$S_{ip} = 3\vec{\sigma}_i\cdot\hat{r}\;\vec{\sigma}_p\cdot\hat{r} - \vec{\sigma}_i\cdot\vec{\sigma}_p$	tensor operator with $\hat{r} = \vec{r}/\lvert\vec{r}\rvert$
$\vec{\sigma}$	Pauli spin matrices.

For small momentum transfer $q < 1\,\mathrm{fm}^{-1}$, the spin-orbit part V^{LS} and the tensor part V^T are small compared to the central part V^C. The central part can be divided up in terms describing non-spinflip, spinflip $\vec{\sigma}_i\cdot\vec{\sigma}_p$, isospinflip $\vec{\tau}_i\cdot\vec{\tau}_p$ and spin-isospinflip $\vec{\sigma}_i\cdot\vec{\sigma}_p\vec{\tau}_i\cdot\vec{\tau}_p$ parts

$$V_{ip}(r_{ip}) = V_0^C(r_{ip}) + V_\sigma^C(r_{ip})\,\vec{\sigma}_i\cdot\vec{\sigma}_p + V_\tau^C(r_{ip})\,\vec{\tau}_i\cdot\vec{\tau}_p + V_{\sigma\tau}^C(r_{ip})\,\vec{\sigma}_i\cdot\vec{\sigma}_p\vec{\tau}_i\cdot\vec{\tau}_p\,, \tag{2.9}$$

which are shown in Fig. 2.2. The iscoscalar spin-independent part V_0^C is the dominating interac-

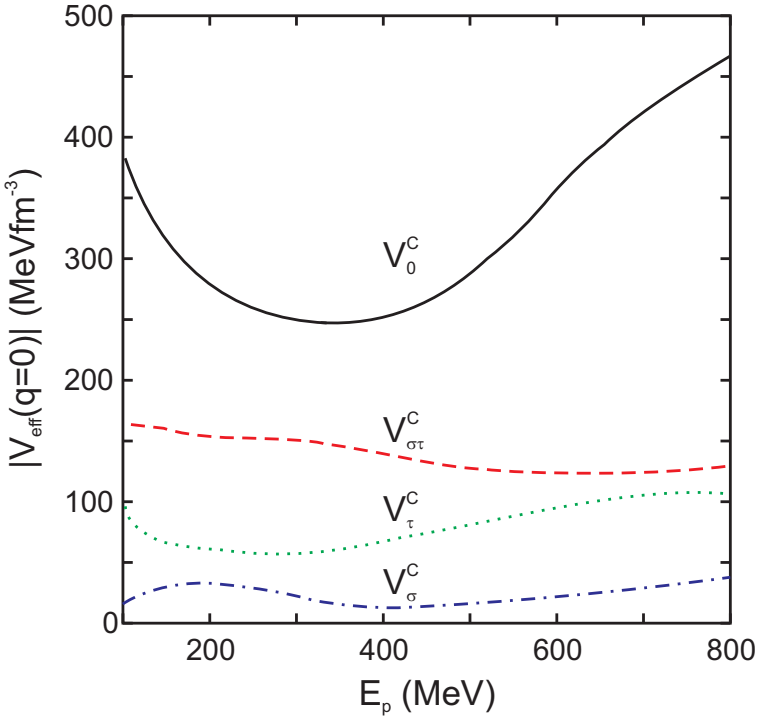

Figure 2.2: Development of the central part of the effective nucleon-nucleus interaction of Franey and Love [23] for E_p from 100 to 800 MeV with vanishing momentum transfer $q \to 0$.

tion but in the energy region of interest at E_p of about 300 MeV it has got a minimum. Furthermore, the isovector spin-independent term V_τ^C has a minimum in the relevant energy regime and the isoscalar spin-dependent part V_σ^C is small over the whole energy range. Therefore, the isovector spin-dependent interaction $V_{\sigma\tau}^C$ is enhanced relative to the other contributions. It mediates $\Delta L = 0$, $\Delta S = 1$, $\Delta T = 1$ (spin-M1) transitions.

2.4 Polarization transfer coefficients

Measurements with polarized beams give access to study the spinflip-character of transitions in nuclei. Reactions of the type

$$\frac{\vec{1}}{2} + A \to \frac{\vec{1}}{2} + B\,, \tag{2.10}$$

where $\frac{\vec{1}}{2}$ depicts a polarized spin-$\frac{1}{2}$ particle, are described in the Plane Wave Impulse Approximation (PWIA). In this framework the t-matrix for the nucleon-nucleus scattering between initial state $|i\rangle$ and final state $|f\rangle$ can be written as

$$T = \left\langle f | M(q) e^{-i\vec{q}\cdot\vec{r}} | i \right\rangle . \tag{2.11}$$

The dependence of the analyzing power for the j-th component of the beam polarization vector A_j, the differential cross section $\frac{d\sigma}{d\Omega}$ and the polarization transfer coefficients (PTC) D_{ij} depend on the t-matrix in the following way [24]

$$A_j = \frac{\mathrm{Tr}(TT^\dagger\sigma_n)}{\mathrm{Tr}(TT^\dagger)}, \qquad \frac{d\sigma}{d\Omega} = \frac{1}{2}\mathrm{Tr}(TT^\dagger), \qquad D_{ij} = \frac{\mathrm{Tr}(T\sigma_j T^\dagger\sigma_i)}{\mathrm{Tr}(TT^\dagger)}. \tag{2.12}$$

The indices i and j denote the direction of the projectile spin in the initial and in the final state, respectively.
The scattering amplitude can be expressed under the energy-on-shell condition in the notation of Kerman, McManus, and Thaler [25] as

$$\begin{aligned} M(q) &= A + B\sigma_{1\hat{n}}\sigma_{2\hat{n}} + C\left(\sigma_{1\hat{n}} + \sigma_{2\hat{n}}\right) + E\sigma_{1\hat{q}}\sigma_{2\hat{q}} + F\sigma_{1\hat{p}}\sigma_{2\hat{p}} \qquad (2.13)\\ &= A + \frac{1}{3}(B+E+F)\vec{\sigma}_1\cdot\vec{\sigma}_2 + C(\sigma_1+\sigma_2)\cdot\hat{n} + \frac{1}{3}(E-B)S_{12}(\hat{q}) + \frac{1}{3}(F-B)S_{12}(\hat{p}). \end{aligned}$$

The momenta $\hat{q}$, $\hat{n}$ and $\hat{p}$ are defined by $\vec{k}$ and $\vec{k}'$ as

$$\hat{q} = \frac{\vec{q}}{|\vec{q}|} \qquad \text{with} \qquad \vec{q} = \vec{k}' - \vec{k}, \tag{2.14}$$

$$\hat{n} = \frac{\vec{n}}{|\vec{n}|} \qquad \text{with} \qquad \vec{n} = \vec{k}' \times \vec{k}, \tag{2.15}$$

$$\hat{p} = \hat{q} \times \hat{n}. \tag{2.16}$$

Each complex amplitude coefficient $A - F$ is given by an isoscalar and an isovector part, e.g. $A = A_0 + A_\tau \vec{\tau}_1 \cdot \vec{\tau}_2$. The terms in Eq. (2.13) correspond to central, spin-dependent, spin-orbit, tensor and tensor-exchange parts of the effective interaction. The central spin-independent component A is zero for spinflip transitions. For 0° measurements the spin-orbit part $C = 0$ and the tensor component $(E - B)$ vanishes as $E = B$ [26]. Under these restrictions polarization transfer oberservables are given by

$$D_{SL} = D_{LS} = 0, \tag{2.17}$$

$$D_{SS} = D_{NN} = \frac{\left(|B_i|^2 - |F_i|^2\right)X_T^2 - |B_i|^2 X_L^2}{\left(|B_i|^2 + |F_i|^2\right)X_T^2 + |B_i|^2 X_L^2}, \tag{2.18}$$

$$D_{LL} = \frac{\left(-3|B_i|^2 + |F_i|^2\right)X_T^2 + |B_i|^2 X_L^2}{\left(|B_i|^2 + |F_i|^2\right)X_T^2 + |B_i|^2 X_L^2} \tag{2.19}$$

including spin-transverse and spin-longitudinal form factors X_T and X_L. The index i indicates the isospin character of the transition. Furthermore the indices S, L and N are linked to the sideway $\hat{s}$, longitudinal $\hat{l}$ and normal $\hat{n}$ axes in the projectile frame depicted in Fig. 2.3. The $\hat{l}$ axes corresponds to the beam direction, $\hat{n}$ is normal to the horizontal plane and $\hat{s}$ complements the right-handed coordinate system. The polarization transfer coefficients D_{SS} and D_{NN} are equal due to the rotational symmetry at 0°. The sum of the diagonal elements is equal to -1 for

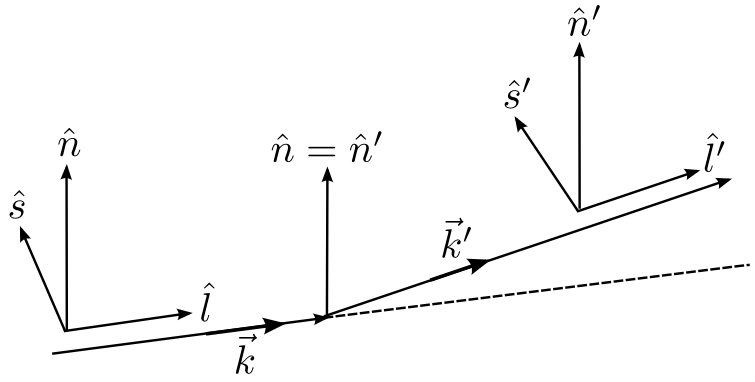

Figure 2.3: Coordinate system in the projectile frame.

spinflip transitions and equal to 3 for non-spinflip transitions at forward angles with negligible spin-orbit part [27]. It is useful to define the total spin transfer Σ [28] as a linear combination of polarization transfer coefficients

$$\Sigma = \frac{3 - (D_{SS} + D_{NN} + D_{LL})}{4}. \tag{2.20}$$

Applying the condition $D_{SS} = D_{NN}$ at 0° the total spin transfer reduces to

$$\Sigma = \frac{3 - (2D_{NN}(\text{or } D_{SS}) + D_{LL})}{4}. \tag{2.21}$$

For $(\vec{p}, \vec{p}')$ experiments at 0° $\left(\hat{l} \approx \hat{l}'\right)$ Σ takes a value of one for spinflip ($\Delta S = 1$) and zero for non-spinflip ($\Delta S = 0$) transitions and this allows to separate spinflip and non-spinflip cross section parts in the continuum region

$$\frac{d\sigma}{d\Omega}(\Delta S = 1) \equiv \Sigma \left(\frac{d\sigma}{d\Omega}\right), \tag{2.22}$$

$$\frac{d\sigma}{d\Omega}(\Delta S = 0) \equiv (1 - \Sigma) \left(\frac{d\sigma}{d\Omega}\right). \tag{2.23}$$

Non-spinflip cross sections can be identified with E1 excitations and spinflip cross sections with spin-M1 excitations refering to the excitation mechanisms presented in the previous sections. This technique has been successfully applied to ^{12}C [29], ^{16}O [24] and ^{208}Pb [30] recently.

3 High-resolution polarized proton scattering experiments at RCNP

3.1 Facility

The high resolution polarized proton scattering experiments were performed at the Research Center for Nuclear Physics (RCNP) in Osaka, Japan. The facility is shown in Fig. 3.1. A po-

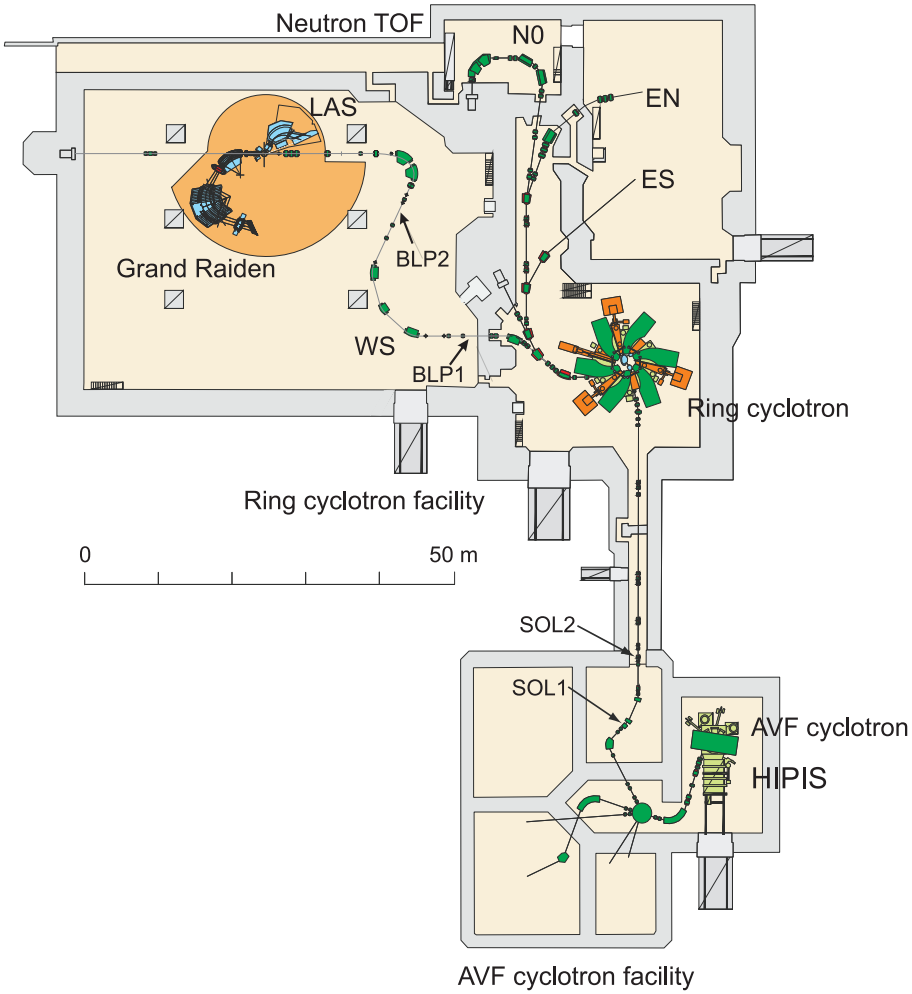

Figure 3.1: Scheme of the experimental facility at the RCNP in Osaka, Japan.

larized proton beam is provided by the High Intensity Polarized Ion Source (HIPIS) utilizing the cold atomic beam technology and an electron cyclotron resonance ionizer [31]. The beam is injected into the Azimuthally Varying Field (AVF) cyclotron where it gets accelerated up to 54 MeV. The spin direction of the proton is reversed every second to eliminate the geometrical asymmetries of the experimental setup. The final energy E_p of 295 MeV is achieved in the RING cyclotron. Two superconducting solenoids (SOL1 and SOL2) are installed in the injection line between the two cyclotrons in order to control the spin axis of the polarized protons. The beam

can be extracted into several experimental halls, where a large diversity of measurements can be performed.
In order to study unstable nuclei, the East-North (EN) [32] beam line is used, whereas the production of ultra-cold neutrons is studied in the East-South (ES) course. Utilizing the North (N0) beam line together with the neutron-TOF setup spin-isospin excitations with (p,n) reactions are measured [33]. In the present experiment the beam is transported via the high-resolution West-South (WS) [34] beamline to the Large Acceptance [35] and Grand Raiden [36] spectrometers. Beam line polarimeters (BLP1 and BLP2) are placed in the WS beamline to control the beam polarization. The functionality of the BLPs is discussed in Sec. 3.4.

3.2 Spectrometers

The experimental setup of the Grand Raiden and the Large Acceptance Spectrometer for 0° measurement with sideway and longitudinal polarized proton beams is illustrated in Fig. 3.2.

3.2.1 Grand Raiden spectrometer

The high resolution spectrometer Grand Raiden (GR) has a complex magnetic structure with a Q1-SX-Q2-D1-MP-D2 configuration. Here, D denotes dipole magnets, Q indicates quadrupoles and SX and MP label sextupole and multipole magnets, respectively. The multipole magnet minimizes higher-order aberrations. Additionally, a third dipole magnet, the dipole magnet for spin rotation (DSR), is used for the D_{LL} measurement with longitudinal polarized beam as shown in the lower part of Fig. 3.2. The spectrometer has a high momentum resolution of $p/\Delta p = 37000$ and a momentum acceptance of 5 %. Further parameters of the Grand Raiden spectrometer are summarized in the left part of Tab. 3.1. The detector system of the Grand Raiden spectrometer consists of two parts: the Focal Plane Detector System (FPDS) and the Focal Plane Polarimeter (FPP).

3.2.2 Large Acceptance Spectrometer

The Large Acceptance Spectrometer (LAS) consists of a quadrupole and a dipole magnet. It provides a momentum resolution of $p/\Delta p = 4980$ and a momentum acceptance of 30 %. A detailed summary of the parameters can be found in the right part of Tab. 3.1. The focal plane detector system of the LAS is formed by pairs of multiwire drift chambers (MWDC) and two planes of plastic trigger scintillation counters. In the present experiment it was placed at 60° throughout the experiment to monitor the vertical position of the beam on the target which is needed for the reconstruction of the scattering angles.

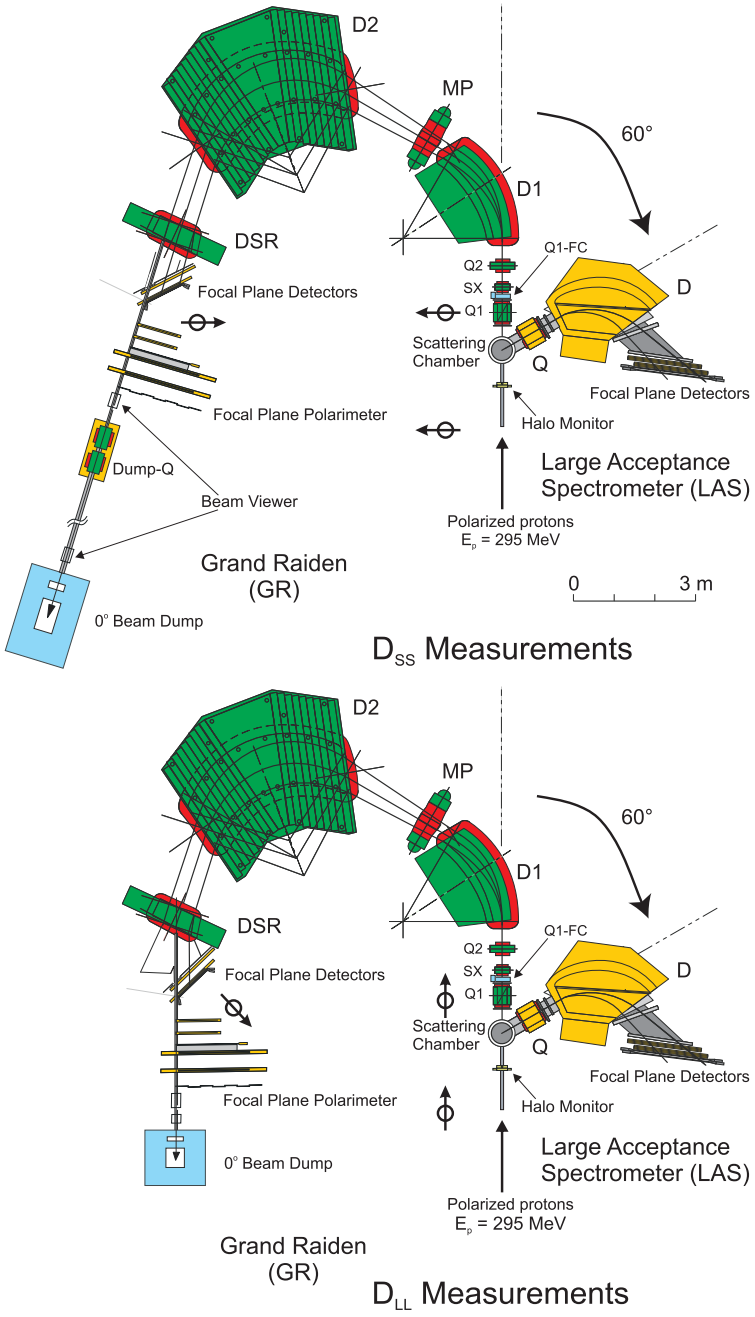

Figure 3.2: Schematic view of the experimental setup for 0° measurement with sideway and longitudinal polarized proton beam.

Table 3.1: Parameters of the Grand Raiden and the Large Acceptance Spectrometers.

	Grand Raiden (GR)	Large Acceptance Spectrometer (LAS)
Configuration	Q1-SX-Q2-D1-MP-D2(-DSR)	QD
Mean orbit radius	3 m	1.5 m
Total deflection angle	162°	70°
Tilting angle of focal plane	45°	57°
Maximum magnetic rigidity	5.4 Tm	3.2 Tm
Momentum range	5 %	30 %
Momentum resolution	37 076	4 980
Horizontal magnification	-0.417	-0.4
Vertical magnification	5.98	-7.3
Acceptance of horizontal angle	±20 mr	±60 mr
Acceptance of vertical angle	±70 mr	±100 mr

3.3 Detector systems

The Focal Plane Detector System (FPDS) [37] and the Focal Plane Polarimeter (FPP) [38] form the two major parts of the Grand Raiden spectrometer detector system sketched in Fig. 3.3. The

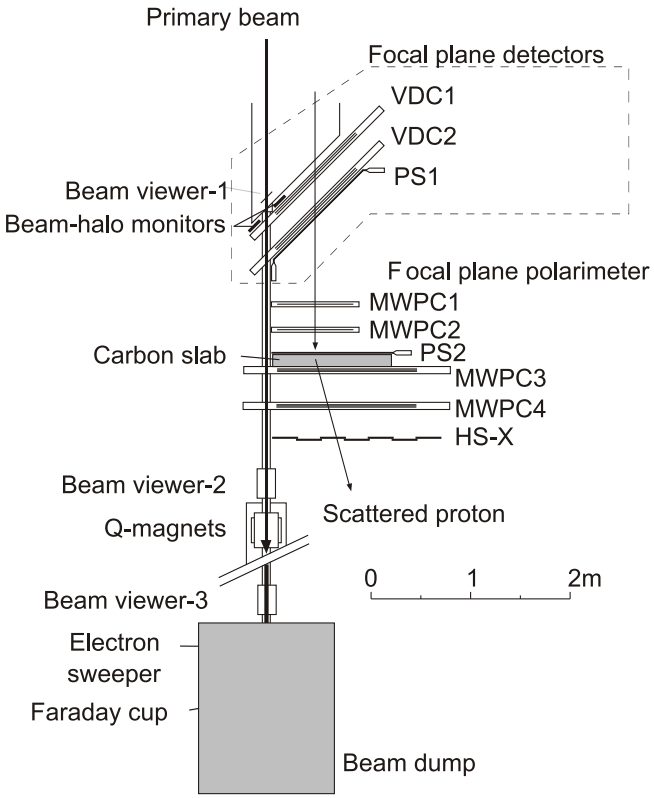

Figure 3.3: Detector system of the Grand Raiden spectrometer and the beam line to the Faraday cup for the 0° measurement.

scattering angle of the particles and the excitation energy is measured utilizing the FPDS. The polarization of scattered protons is determined by the FPP.

3.3.1 Focal plane detector system

The FPDS consists of two sets of vertical drift chambers (VDCs) and a plastic scintillator (PS1) as a trigger detector. The sensitivity to the position and the scattering angle of particles makes multiwire drift chambers a well-suited tool for the reconstruction of trajectories. VDC1 and VDC2 measure the four parameters x_{fp}, θ_{fp}, y_{fp} and ϕ_{fp} of the scattered protons. Here, x_{fp} and θ_{fp} are intersection point and intersection angle of the particle in the focal plane, whereas y_{fp} and ϕ_{fp} denote those in the non-dispersive plane of the system.
Each VDC is built up of X and U anode wire planes sandwiched between three chathode planes. In the X plane wires are fixed perpendicular to the dispersion direction of the Grand Raiden spectrometer whereas in the U plane wires are tilted by an angle of $\pm 48.19°$ towards the X plane wires. The drift chambers were filled with a gas mixture composed from argon (71 %), iso-butane (29 %) and iso-propyl-alcohol.
The plastic scintillator PS1 with a thickness of about 3 mm serves to determine the energy loss of scattered protons for particle identification. Moreover, the thickness of the PS1 is adjusted so that the secondary scattering angle in the carbon slab can be determined with sufficient accuracy.

3.3.2 Focal plane polarimeter

Secondary scattering events arise from scattering at a carbon slab which is 9 cm thick with a density of $1.7\,\mathrm{g/cm^3}$ in the Focal Plane Polarimeter system. If a polarized particle passes through the carbon analyzer the spin-orbit interaction between the projectile and the ^{12}C nucleus causes an azimuthal asymmetry in the scattering process. The reconstructed spin-transfer matrix of the spectrometer and the measured asymmetry in the focal plane determine the polarization of the protons at the initial reaction point. The multiwire proportional chambers MWPC1 and MWPC2 placed before the carbon slab consist each of only X plane. They are used as a second-level trigger. The plastic scintillator (PS2) in front of the carbon analyzer is used as a trigger, too. Chambers MWPC3 and MWPC4 located behind the carbon analyzer additionally include U and V anode wire planes tilted by $-45°$ and $+45°$ relative to the X plane and determine both x and y trajectories of secondary scattered protons. All MWPC chambers were filled with a mixture of argon (66 %), iso-butane (33 %) and freon (0.3 %). The hodoscope also used as a trigger contains two parts: HS-X which includes eight plastic scintillation detectors and HS-Y which consists of five plastic scintillators. The HS-Y and one detector from the HS-X were removed in order to enable the installation of the beam duct for the 0° measurement.

3.4 Beam polarization

The polarization of the protons is monitored by two beam line polarimeters (BLP1 and BLP2) placed in the WS beam line. In the left part of Fig. 3.4 the horizontal part of a BLP is shown from top view. It consists of two (left and right) pairs of plastic scintillation counters measuring the

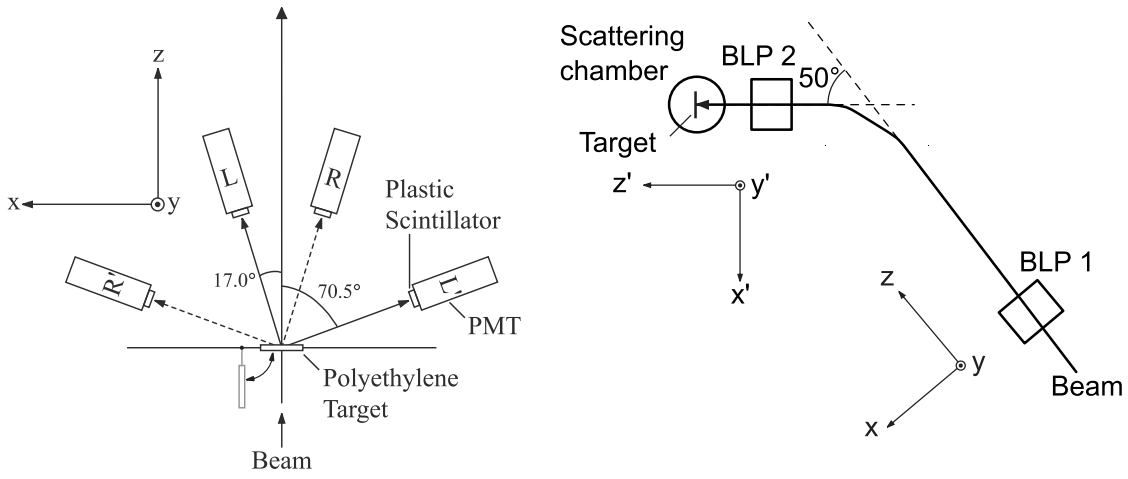

Figure 3.4: The left figure shows the horizontal part of a beam line polarimeter for polarized proton scattering at $E_p = 295\,\mathrm{MeV}$ from top view. The right figure depicts the setup for the determination of the longitudinal beam polarization.

left-right asymmetry of scattering off an analyzer target. The $(CH_2)_n$ foil with an areal density of $3.5\,\mathrm{mg/cm^2}$ is moved periodically into the beam. The up and down pairs are located in the vertical plane determining up-down asymmetry. Elastic scattering on hydrogen and quasielastic on carbon, which have the same kinematics are measured in coincidence with recoiling protons from the target. The angles under which the detectors are placed are adjusted to the beam energy and the effective analyzing power A_y^{BLP}. The transverse polarization $p_N^{\uparrow(\downarrow)}$ is determined from

$$p_N^{\uparrow(\downarrow)} = \frac{1}{A_y^{BLP}} \frac{N_L^{\uparrow(\downarrow)} - N_R^{\uparrow(\downarrow)}}{N_L^{\uparrow(\downarrow)} + N_R^{\uparrow(\downarrow)}}, \tag{3.1}$$

where $N_L^{\uparrow(\downarrow)}(N_R^{\uparrow(\downarrow)})$ denote the number of coincident events in the L-L′(R-R′) detector pairs with beam spin orientation $\uparrow(\downarrow)$. The second transverse component $p_S^{\uparrow(\downarrow)}$ is derived in analogy from $N_U^{\uparrow(\downarrow)}$ and $N_D^{\uparrow(\downarrow)}$. The longitudinal component is determined by a combination of two BLPs and a deflecting magnet as shown in the right part of Fig. 3.4. The spin precession in the magnet allows to determine the longitudinal component of the beam polarization.

3.5 Beam tuning

For inelastic scattering experiments at forward angles including 0° a high quality beam is required. For instance, a beam halo gives rise to a large amount of background events in the detectors. A stable single-turn beam extraction from both AVF and RING cyclotron has to be achieved for a high quality of the beam. During the experiments, after single-turn extraction from the RING cyclotron the beam is transported to the target via the WS beam line. First, in 2009 a sideway polarized beam was adjusted by changing the magnetic fields of SOL1 and SOL2. Afterwards the polarization axis was rotated in the horizontal plane. This process was monitored by the beam line polarimeters. After polarization tuning an achromatic transport mode was used looking at elastic scattering on ^{197}Au at 8°. The proton beam was tuned to achieve the smallest energy spread. Halo-free tuning of the beam was performed next. After delivering the beam to the 0° beam dump, accelerator elements were tuned to achieve a trigger counting rate on the PS1 as small as possible without a target. A rate of $10-15$ Hz was realized for a 1 nA beam. The dispersion matching [39] conditions were achieved by making use of the faint beam technique after realising a halo-free beam, dispersive transportation was set up. Thus, the full profile of the beam can be seen in the focal plane detectors. Angular and lateral dispersion matching conditions were gained by adjusting the quadrupole fields in the WS course to reduce the spatial and angular spread of the primary beam at the focal plane. An energy resolution of about 10 keV could be achieved. In order to keep the matching conditions during the experiment the fields of all magnets, except the dipoles, in the WS beam line were fixed.

3.6 Ion optics of the Grand Raiden spectrometer

3.6.1 Underfocus mode

Track reconstruction of the scattered particles from the focal plane back to the target position is very important for obtaining good angular resolution. In 0° measurements the relation between the scattering angle in the horizontal (dispersive) and in the vertical (non-dispersive) plane is given by

$$\theta_{fp} = \sqrt{A_I^2 + B_I^2}, \tag{3.2}$$

where θ_{fp} denotes the total scattering angle at the focal plane whereas A_I and B_I stand for the horizontal and the vertical scattering angle at the target, respectively. With normal field settings of the Grand Raiden spectrometer magnets, vertical and horizontal trajectories of the scattered particles are focused at the focal plane. Due to the small vertical magnification factor

of the Grand Raiden spectrometer of 5.98 (cf. Tab. 3.1) the vertical scattering angle resolution gets worse than 20 mrad. With this configuration a large part of the vertical angle acceptance of the spectrometer is lost. This is not the case for a vertical overfocus or underfocus mode which can be applied by changing the magnetic field of the quadrupole Q1 of the Grand Raiden spectrometer [40]. During the experiment an underfocus mode was chosen because of the larger horizontal and vertical scattering angle correlation at the focal plane in an overfocus mode. Therefore, the magnetic field of Q1 quadrupole was decreased by 6 % relative to the normal focus mode.

3.6.2 Scattering angle calibration

The ion optics of the Grand Raiden spectrometer make it necessary to perform a calibration in order to reconstruct scattering angles at the target position from the scattering information gained by the focal plane detectors. Therefore sieve slit measurements were performed inserting a 5 mm thick brass plate shown in Fig. 3.5 with 25 holes at the entrance of the Grand Raiden spectrometer 638 mm downstream of the target position. This technique allows to relate the vertical position and the scattering angle at the focal plane to the scattering angle at the target position based on the distance between the holes in the sieve slit and the target. The

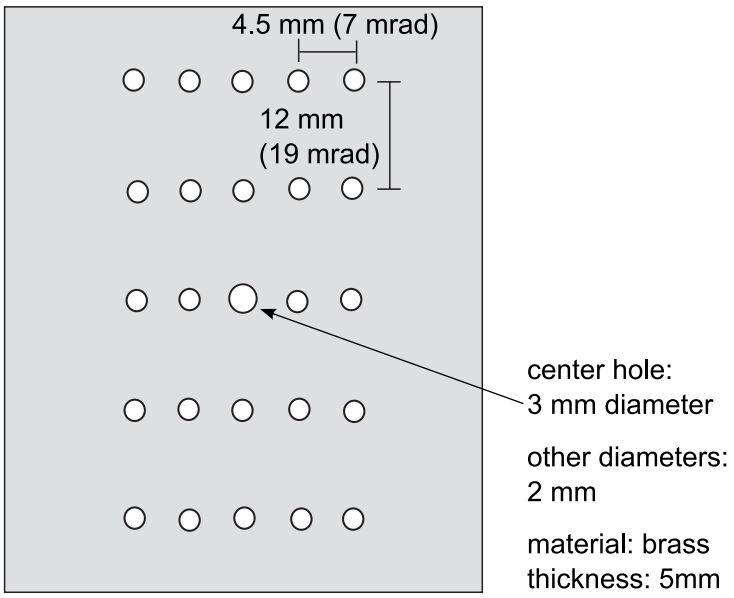

Figure 3.5: Schematic view of the sieve slit.

central hole has got a diameter of 3 mm (4.7 mrad) while the other holes are 2 mm (3.1 mrad) in diameter. The distance between two horizontal holes is 4.5 mm (7 mrad) and between two vertical holes 12 mm (19 mrad), respectively. For the elastic scattering measurements in 2009 the Grand Raiden spectrometer was set to an angle of 15.2°. A ^{58}Ni foil with an areal density of 100 mg/cm^2 was used as target. To determine the influence of the horizontal position

at the focal plane on the scattering angle, the magnetic fields of all magnets were changed by +1.2 %, +1.8 %, +2.6 %, +3.4 % and +4.2 % relative to the standard underfocus setting of the ion optics. With these magnetic settings the horizontal position at the focal plane of elastically scattered protons corresponds to excitation energies of about 6, 10, 14, 18, 22 MeV for inelastically scattered protons under 0° covering the full excitation energy range. In order to take into account the beam position on the target, measurements were done with the beam spot at the center and vertically shifted by ±1 mm. So, all in all fifteen data runs were taken during the sieve slit measurement. The determination of the scattering angles based on these data is presented in Sec. 4.2.

4 Data analysis

In the following sections data analysis steps and the extraction of polarization transfer coefficients are presented utilizing the programm code ANALYZER [41] developed at RCNP for processing of data from the LAS and the Grand Raiden spectrometer. This code makes use of HBOOK and PAW++ packages from the CERN libraries [42]. The following steps in the data reduction process

- conversion from drift time to drift length,
- calibration of scattering angles,
- correction of higher-order aberrations of the Grand Raiden spectrometer,
- excitation energy calibration,
- background subtraction, and
- beam polarization determination

are described for the example of the ^{120}Sn experiment E316 [43] performed in November 2009 in the following sections. In Tab. 4.1 all target information is summarized. The data reduction process was already completed for the 2006 and 2008 measurements.

Table 4.1: Summary of the targets used for measurements in different experiments.

target	areal density [mg/cm^2]	isotopical enrichment [%]	experiment (aver. polarization)
^{208}Pb	5.2	≥ 99	2006 (0.735), 2008 (0.671)
^{197}Au	1.68		beam tuning 2009
^{120}Sn	6.5	98.39	2008 (0.659), 2009 (0.712)
^{58}Ni	100.1		sieve-slit measurements 2009
^{27}Al	3.74		excitation energy calibration 2009
^{12}C	30		2008, 2009

4.1 Conversion from drift time to drift length

The intersection points and the intersection angles in the focal plane of the Grand Raiden spectrometer are determined by two sets of VDCs and a plastic scintillator (PS1) as a trigger. The wire configuration and the working principle of a VDC chamber at the Grand Raiden spectrometer is illustrated in Fig. 4.1. The VDC includes two cathode foils and anode wires which can be

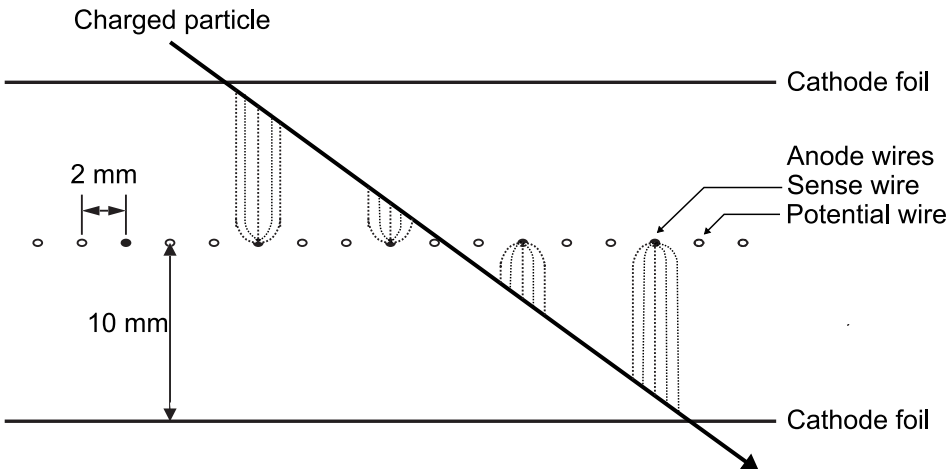

Figure 4.1: Schematic layout of a vertical drift chamber at the Grand Raiden spectrometer. A track of a charged particle passing the detector is shown. Due to the applied electric field electrons drift along the field lines, indicated as dotted lines, from the point of ionization to the sense wires.

divided in sense (signal) and potential (field) wires. A high voltage is applied to the potential wires which are used to form a homogeneous electric field distribution, whereas sense wires are kept at ground potential. When a charged particle passes the detector colliding with molecules and atoms of the filling gas electron-ion-pairs are created. Due to the applied electric field the electrons are accelerated towards the anode plane moving with an almost constant drift velocity of about 5 cm/μs. Therefore the electron drift time is proportional to the distance from the point of ionization to the anode wire.

The time difference measured by a Time-to-Digital Convertor (TDC) between the anode wire signal and the delayed signal from the plastic scintillator has to be converted to a drift length for the track reconstruction. On the left hand side of Fig. 4.2 the conversion from drift time to drift length is shown. The drift length spectrum has a flat distribution. The right part illustrates the relation between the TDC channel numbers and the drift length. Due to the inhomogeneous electric field close to the anode wires, deviations occur for short drift times corresponding to high TDC channels.

The angle between the primary beam axis and the VDCs is 45° as shown in Fig. 3.3. Therefore particles create signals at more than two wires along their trajectory. Events with signal in neighboring wires are considered as a cluster while single wire signals are rejected. Moreover, the wire with the shortest drift time is neglected as the electric field near the sense wires is not uniform leading to uncertainties in the conversion from drift time to drift length. It is also assumed that each plane contains only one cluster. The intersection point at the wire plane is calculated by a least-square fit from the drift length of the signal wires. The intersection angle and the full trajectory is obtained by combining the information from all wire planes.

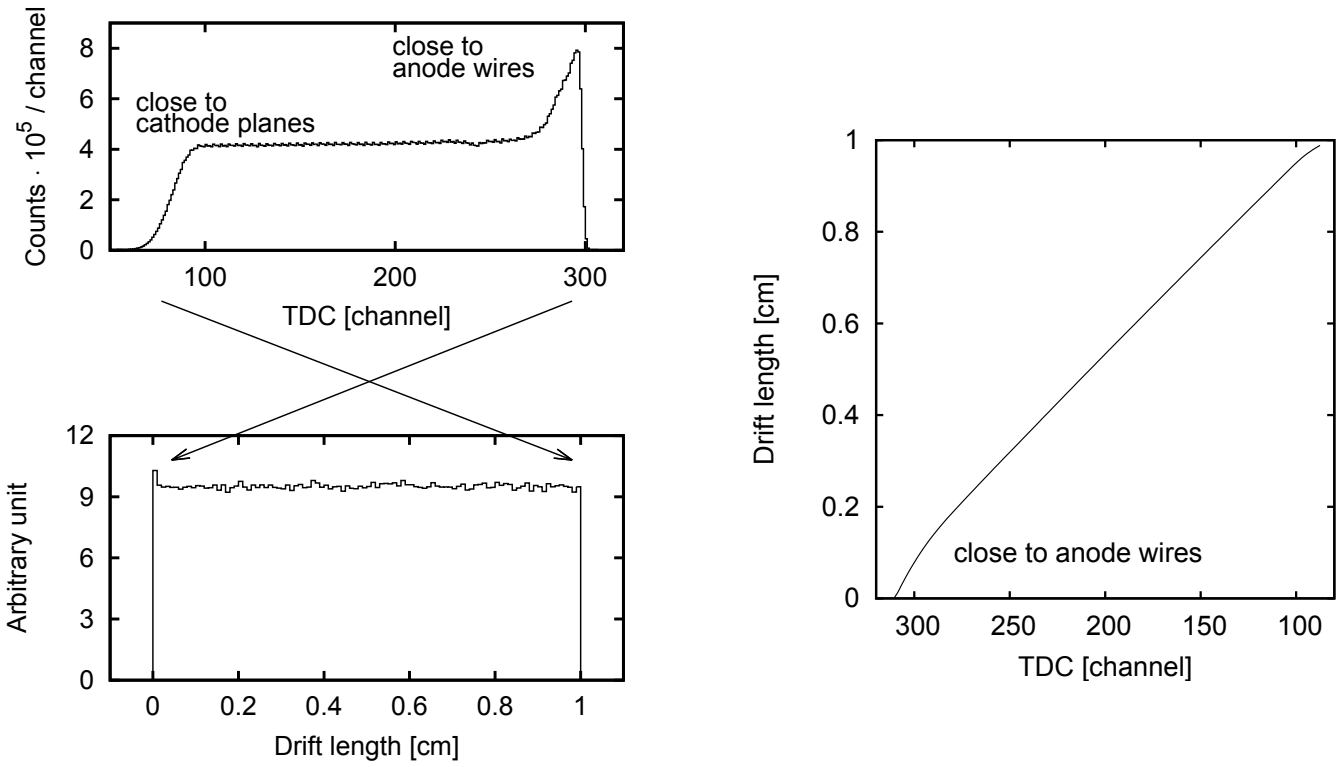

Figure 4.2: Conversion from drift time to drift length for the vertical drift chambers at the Grand Raiden spectrometer. The spectra of the VDC2 U plane are shown as an example.

4.2 Calibration of scattering angles

The calibration of horizontal and vertical scattering angles at the target A_I and B_I using the data from the sieve slit measurements described in Sec. 3.6.2 is performed in this section. The horizontal scattering angle A_I at the target position is predominantly depending on the horizontal incident angle θ_{fp} at the focal plane, whereas the vertical scattering angle B_I is most sensitive to the vertical position y_{fp} at the focal plane. Furthermore correlations including the intersection point x_{fp} at the focal plane, the intersection angle ϕ_{fp} in the non-dispersive plane and the vertical position y_{LAS} of the beam on the target need to be included.

Elastic scattering events in Fig. 4.3(a) are selected by a gate on x_{fp} indicated by the grey band. The bump around $x_{fp} = -20\,\text{mm}$ can be identified as elastic scattering events which are passing through the brass plate with an energy loss of 10 MeV. The vertical beam position on the target monitored by the LAS is depicted in Fig. 4.3(b). Including these information a two-dimensional plot in the $y_{fp} - \theta_{fp}$ plane can be defined as illustrated in Fig. 4.3(c). The two coordinates of the center of the spots are gained by slicing the histogram in horizontal(vertical) direction and projecting these slices on the $y_{fp}(\theta_{fp})$ axis. Assuming a round shape of the hole images, the central positions can be determined employing Gaussian fits shown in the bottom(left) plot of Fig. 4.3(c). Scattering at the opening of the sieve slit holes can be neglected. To establish the values of ϕ_{fp}, the two-dimensional histogram $y_{fp} - \phi_{fp}$ shown in Fig. 4.3(d) is analyzed. The central positions are obtained by applying gates on elastic events and choosing a specific θ_{fp}

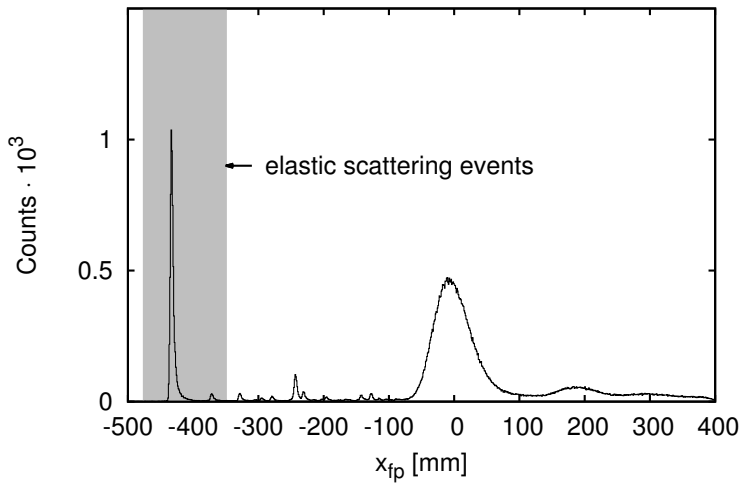

(a) Gate on elastic scattering events.

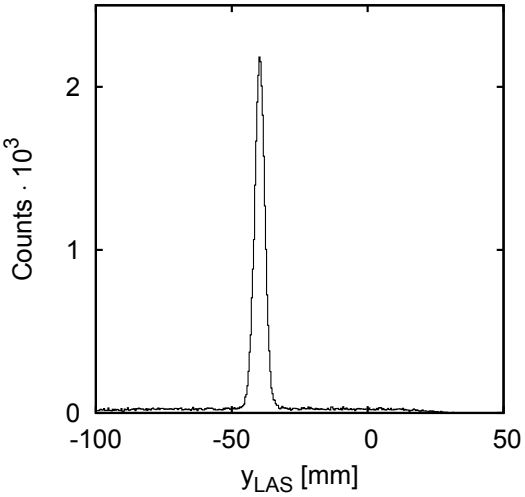

(b) Vertical position of the beam on the target monitored by LAS.

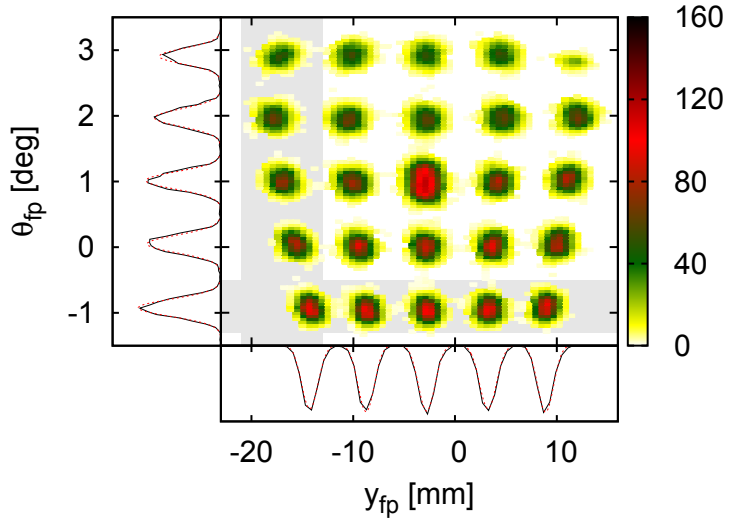

(c) Horizontal scattering angle at the focal plane θ_{fp} as a function of y_{fp}.

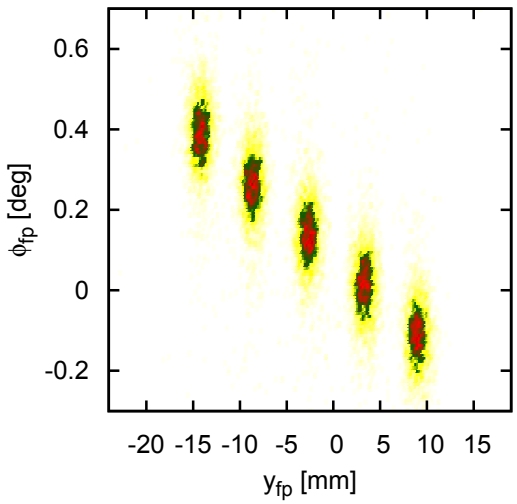

(d) Vertical scattering angle at the focal plane ϕ_{fp} as a function of y_{fp}.

Figure 4.3: Extraction of y_{LAS}, θ_{fp}, y_{fp} and ϕ_{fp} from the sieve slit analysis.

region. Afterwards, the events are projected on the ϕ_{fp}- axis and Gaussian fits are utilized. Combining all these above mentioned information, the horizontal and vertical scattering angle

at the target A_I and B_I are determined by a multi-dimensional least-square fit procedure utilizing the GNU scientific library [44] based on the relations

$$A_I(x_{fp},\theta_{fp}) = \sum_{i=0}^{1}\sum_{j=0}^{1} a_{ij}\cdot x_{fp}^{i}\ \theta_{fp}^{j}, \tag{4.1}$$

$$B_I(x_{fp},\theta_{fp},y_{fp},\phi_{fp},y_{LAS}) = \sum_{i=0}^{1}\sum_{j=0}^{1}\sum_{k=0}^{1}\sum_{l=0}^{1} b_{ijkl}\cdot x_{fp}^{i}\ \theta_{fp}^{j}\ y_{fp}^{k}\ \phi_{fp}^{l} + \sum_{i=0}^{1} b_{Li}\cdot x_{fp}^{i}\ y_{LAS}\,.$$

Here, a_{ij}, b_{ijkl} and b_{Li} denote fit parameters whose numerical values are summarized in Tab. 4.2. Previous studies [45] pointed out that the coefficients of y_{fp} and mixed terms for the horizontal scattering angle at the target A_I are orders of magnitude lower than the first order contributions from x_{fp} and θ_{fp}. As a consequence simplified functions presented in Ref. [14] are used in the fitting procedure. The reconstruction of the sieve slit holes with the scattering angle calibration based on Eqs. (4.1) is depicted in Fig. 4.4 for different magnetic field settings corresponding to excitation energies E_x of about 6, 14 and 18 MeV, respectively. Uncertainties

Table 4.2: Table of coefficients from the fit of Eqs. (4.1) for the reconstruction of the scattering angles. The numbers of i, j, k and l represent the exponent of x_{fp}, θ_{fp}, y_{fp} and ϕ_{fp}, respectively.

$i\,j$	coefficients a_{ij}
00	$1.739\cdot10^{-2}$
01	$-4.266\cdot10^{-1}$
10	$2.331\cdot10^{-5}$

$i\,j\,k\,l$	coefficients b_{ijkl}
0000	$-5.301\cdot10^{-2}$
0001	3.625
0010	$-1.885\cdot10^{-3}$
1000	$4.164\cdot10^{-5}$

i	coefficients b_{Li}
0	$-1.116\cdot10^{-3}\cdot y_{LAS}$
1	$6.282\cdot10^{-7}\cdot y_{LAS}$

in the determination of the scattering angles are estimated from the average deviation from the correct values for the spot centers indicated by the crossing points of the black dashed lines in the right part of Fig. 4.4. For horizontal and vertical scattering angles uncertainties of less then 0.1° and 0.3°, respectively, are determined.

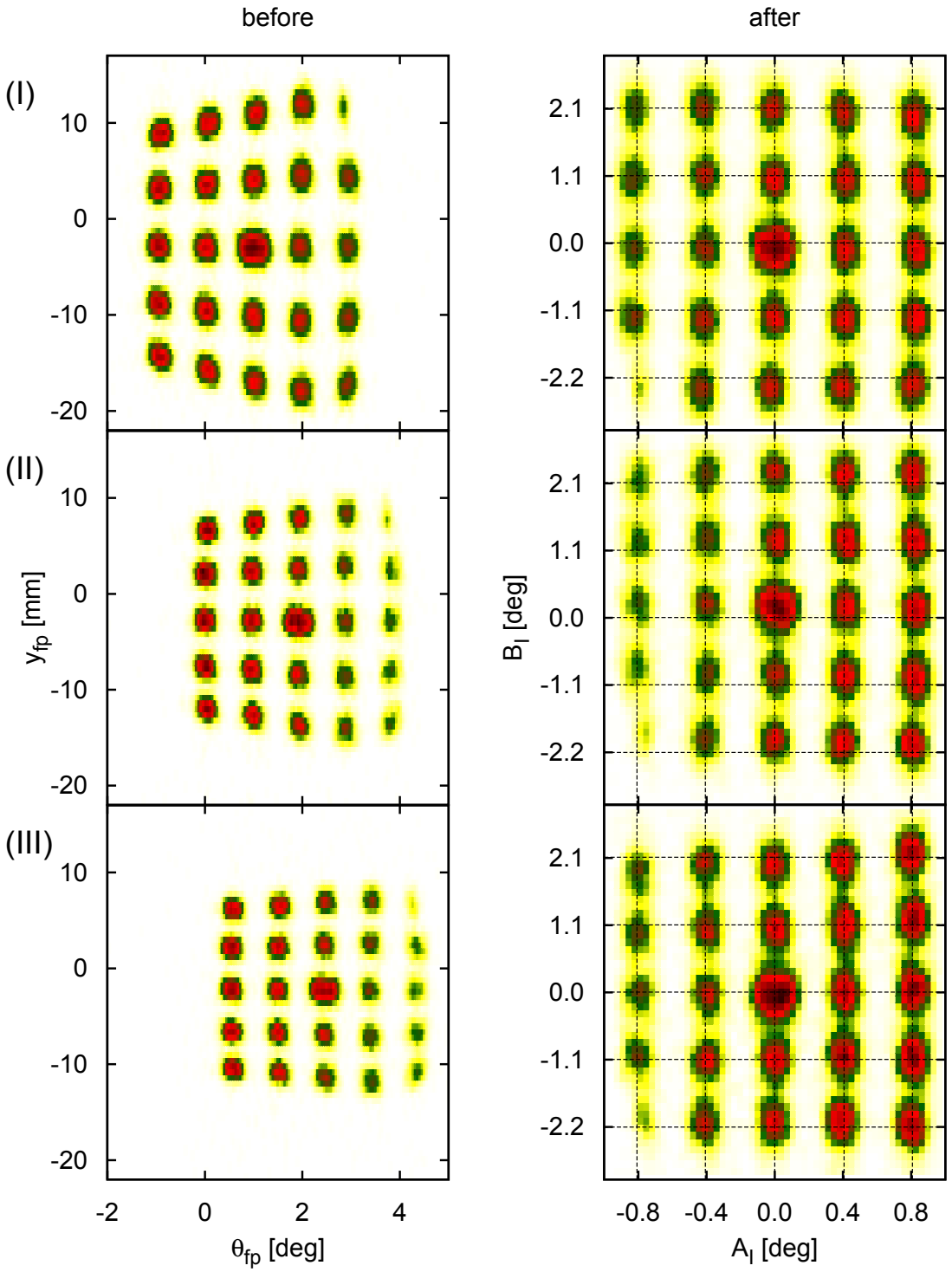

Figure 4.4: Two-dimensional $y_{fp} - \theta_{fp}$ histograms before and after scattering angle calibration due to Eqs. (4.1) utilizing the parameters of Tab. 4.2. The images (I), (II) and (III) correspond to excitation energies of $6, 14$ and $18\,\mathrm{MeV}$, respectively. The black dashed lines illustrate the position of the actual holes in the sieve slit, providing a measure for the uncertainty of the angle reconstruction.

4.3 Correction of higher-order aberrations of the Grand Raiden spectrometer

To obtain an optimum energy resolution the correction of higher-order aberrations of the Grand Raiden spectrometer is necessary. Assuming elastic scattering on ^{12}C and a proton beam energy of 295 MeV the kinematical dependence on the scattering angle was calculated with the program KINMAT [46]. It is well reproduced by a fit function

$$E(\theta_{lab}) = -8.7 \cdot 10^{-3}\, \theta_{lab}^2 \text{ MeV/deg}^{-2} + 295 \text{ MeV} \tag{4.2}$$

as shown in Fig. 4.5. After correcting for this effect, there remain other kinematic correlations

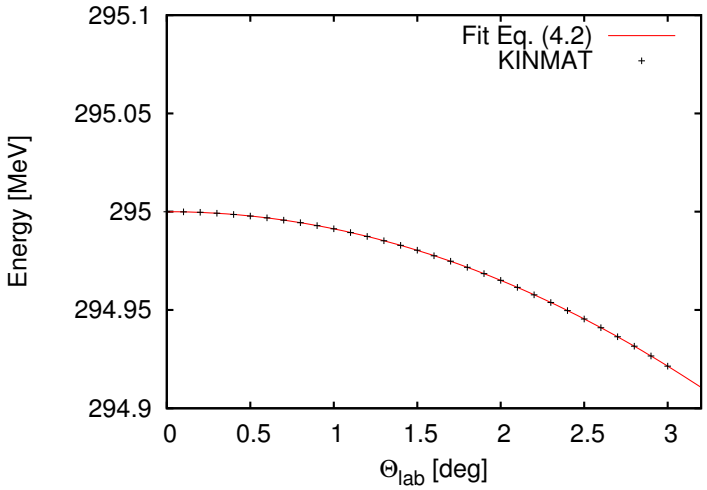

Figure 4.5: Fit of the kinematical dependence on the scattering angle θ_{lab} determined by Eq. 4.2.

due to the ion-optical properties of the Grand Raiden spectrometer. In particular, the intersection points x_{fp} show a correlation with the values of θ_{fp} and y_{fp}. This is eliminated by the following procedure: A measurement with a ^{12}C target at 0° was performed exciting well known discrete transitions at 7.65, 12.71 and 15.1 MeV. These states are slightly curved in the $x_{fp} - \theta_{fp}$ plane as shown in the upper part of Fig. 4.6. By analyzing the $x_{fp} - y_{fp}$ spectra, the dependence on y_{fp} is estimated to be small. The corrected positions x_c can thus be determined by a least-square fit

$$x_c = \sum_{i=0}^{1} \sum_{j=1}^{4} c_{ij} \cdot x_{fp}^i\, \theta_{fp}^j, \tag{4.3}$$

where the indices i and j denote the order of the polynomial used. The results of the fit parameters c_{ij} are summarized in Tab. 4.3. The lower part of Fig. 4.6 illustrates the $x_c - \theta_{fp}$ correlation in the plane after the correction.

Table 4.3: Table of coefficients from the fit of Eq. (4.3) for the correction of x_{fp}. The numbers of i and j represent the exponent of x_{fp} and θ_{fp}, respectively.

$i\,j$	coefficients c_{ij}
01	$-2.220 \cdot 10^{2}$
02	$6.862 \cdot 10^{3}$
03	$-1.229 \cdot 10^{5}$
04	$7.510 \cdot 10^{5}$
11	$-4.649 \cdot 10^{-1}$
12	$1.495 \cdot 10^{1}$
13	$-2.405 \cdot 10^{2}$
14	$1.067 \cdot 10^{3}$

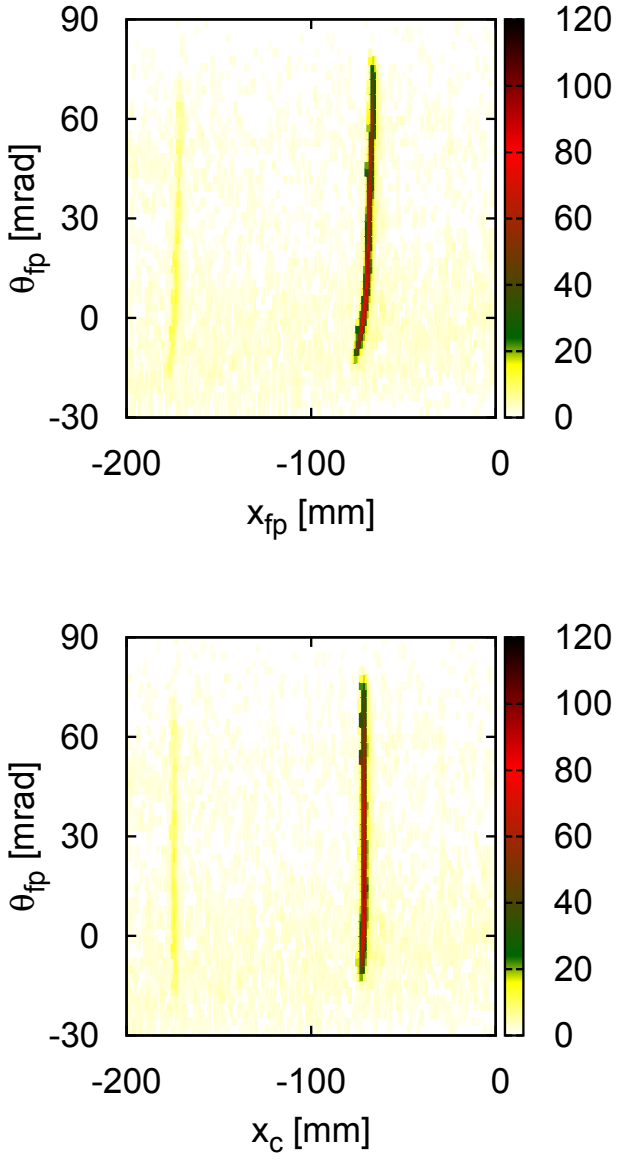

Figure 4.6: Two-dimensional histograms of the $x_{fp} - \theta_{fp}$ plane before and after the x_c correction due to Eqs. (4.3) utilizing the parameters of Tab. 4.3. Applying the corrections straightens the lines of excited states.

4.4 Excitation energy calibration

After the x_c correction an excitation energy calibration was performed. It was based on measurements of states in ^{27}Al. Therefore 7 peaks from a ^{27}Al(p,p') spectrum at 0° gained in a previous experiment [41] have been fitted using the programm HDTV [47]. A polynomial dependence of the excitation energy on x_c was assumed. Taking into account slight shifts in the beam energy or position from run to run the energy calibration has to be performed for each run individually. To obtain a summed spectrum these shifts must be corrected. One way is to normalize all spectra to a prominent peak. In ^{208}Pb, for example, the strong peak at 5.512 MeV is used. For ^{120}Sn this technique is not feasible. So the determination of the excitation energy shifts is based on Pearson's correlation coefficient

$$r_{xy} = \frac{cov(x,y)}{\hat{\sigma}_x \hat{\sigma}_y} = \frac{\sum_{i=1}^{n}(x_i - \bar{x})(y_i - \bar{y})}{\sqrt{\sum_{i=1}^{n}(x_i - \bar{x})^2}\sqrt{\sum_{i=1}^{n}(y_i - \bar{y})^2}}. \tag{4.4}$$

for normalized spectra. Here, $\hat{\sigma}_x$, $\hat{\sigma}_y$ denote the standard deviation and $\bar{x}$, $\bar{y}$ stand for the mean value of the data sets x, y. This calculation is performed utilizing the Mathematica function Correlation[v_1,v_2] providing Pearson's correlation coefficient between data sets v_1 and v_2 which must be of equal length [48]. The set of correlation coefficients obtained is plotted in

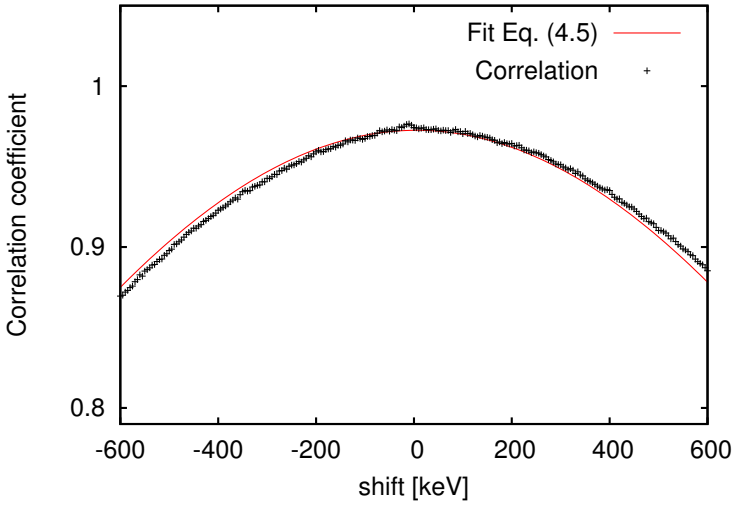

Figure 4.7: Calculation of the Pearson's correlation coefficient and performing a fit due to (4.5) in order to determine excitation energy shift of each run.

Fig. 4.7 and can be well described by a function

$$C = a \cdot e^{-b\cdot(x-x_0)^2}\ , \tag{4.5}$$

where x_0 indicates the excitation energy shift in keV. Furthermore, the $(\vec{p},\vec{p}')$ data can be compared to a NRF experiment [7]. For that purpose the (γ,γ') spectrum which has a superior energy resolution of a few keV was folded with a Gaussian of the width $\Delta E = 30\,\text{keV}$ (FWHM). This corresponds to the energy resolution in the polarized proton scattering experiment. Fig. 4.8 shows the folded $^{120}\text{Sn}(\gamma,\gamma')$ spectrum and a $^{120}\text{Sn}(\vec{p},\vec{p}')$ spectrum obtained after correlation. The spectra are normalized in an energy range from 5.34 MeV to 7 MeV. Both spectra agree

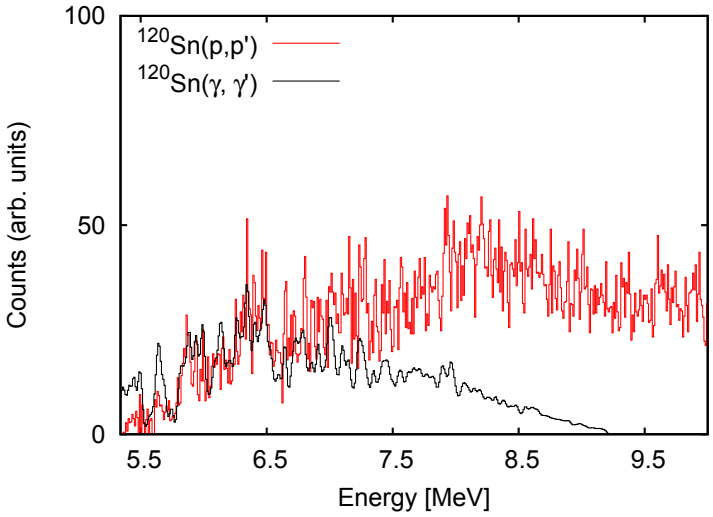

Figure 4.8: A background-subtracted $^{120}\text{Sn}(\vec{p},\vec{p}')$ run after correlation to a $^{120}\text{Sn}(\gamma,\gamma')$ spectrum. The spectra are normalized in an energy range from 5.34 MeV to 7 MeV.

well up to an energy of 7.4 MeV suggesting that transitions in $(\vec{p},\vec{p}')$ are indeed due to Coulomb excitation. The strong deviations at higher energies may result from strong branchings to states other than the ground state or from the sensitivity limit in the NRF experiment. Furthermore, contributions from spinflip M1 transitions in the $(\vec{p},\vec{p}')$ scattering have to be taken into account.

4.5 Background subtraction

Instrumental background events still remain in measured spectra despite the extensive beam tuning. They arise mainly from multiple scattering of the protons in the target material. The statistical nature of multiple scattering is the reason that these events show a flat distribution in the non-dispersive focal plane. True events are focused around y_{fp} and therefore can be distinguished from background events. Thus, a transformation of the coordinates in the non-dispersive $\phi_{fp} - y_{fp}$ plane is performed utilizing a least-square fit method. The relation

$$y_c = y_{fp} + \sum_{i=0}^{1}\sum_{j=0}^{1}\sum_{k=0}^{1} d_{ijk}\cdot x_{fp}^{i}\ \theta_{fp}^{j}\ \phi_{fp}^{k} + d_L\cdot y_{LAS} \tag{4.6}$$

includes dependencies on x_{fp}, θ_{fp} and the vertical position of the beam on the target y_{LAS}. d_{ijk} and d_L denote fit parameters whose values are summed up in Tab. 4.4. The fit procedure

Table 4.4: Table of coefficients from the fit of Eq. (4.6) for the correction of y_{fp}. The numbers of i, j and k represent the exponent of x_{fp}, θ_{fp} and ϕ_{fp}, respectively.

$i\,j\,k$	coefficients d_{ijk}
000	$4.190 \cdot 10^{1}$
001	$1.498 \cdot 10^{3}$
010	$-2.684 \cdot 10^{1}$
011	$9.691 \cdot 10^{3}$
100	$1.245 \cdot 10^{-2}$
101	-3.704
111	$-1.256 \cdot 10^{1}$

coefficient d_L
$1.049 \cdot y_{LAS}$

also uses data obtained during the sieve slit measurements. The results of the transformation in comparison to the uncorrected histograms are depicted in Fig. 4.9. True events are focused at $y_c = 0$ while the distribution of background events is almost flat. Thus, the largest part of the background events is removed by applying a narrow y_c-gate around $y_c = 0$. Moreover, the contribution of background under the true peak is estimated from the counts in the pure background regions on both sides of the peak. However, using this "conventional method" [14] there remain correlations of y_c with B_I (cf. Eq. (4.1)). Taking into account that B_I is not a simple linear function one has to estimate the background as a function of the excitation energy for a given angle cut. In order to eliminate this dependence on the scattering angle an "extended method" is applied. A transformation similar to y_{fp} is performed for ϕ_{fp}

$$\phi_c = \phi_{fp} + \sum_{i=0}^{1} e_i \cdot y_{fp}^{i} \,. \tag{4.7}$$

The values for the fitting parameters e_i are given in Tab. 4.5 and the resulting $\phi_c - y_c$ plot is depicted in Fig. 4.10(a). In order to avoid ambiguities in the background correction caused

Table 4.5: Table of coefficients from the fit of Eq. (4.7) for the correction of ϕ_{fp}. The numbers of i represent the exponent of y_{fp}, respectively.

i	coefficients e_i
0	$-2.391 \cdot 10^{-3}$
1	$-2.443 \cdot 10^{-4}$

by complex correlations among software gates, the basic idea of the new method is to utilize

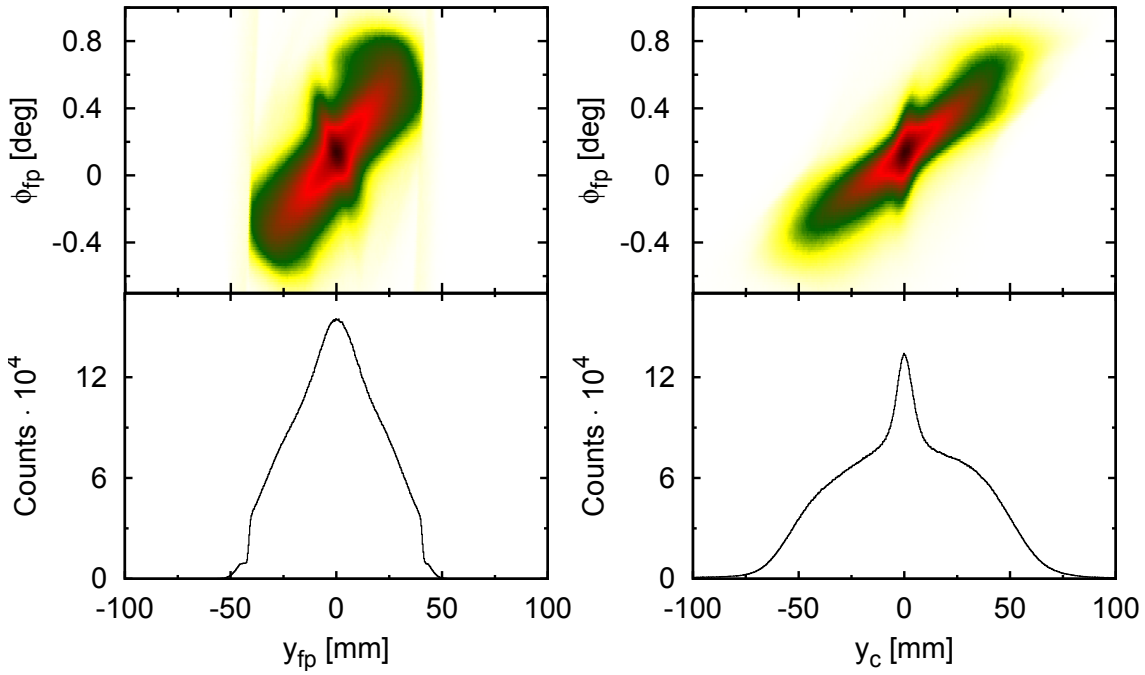

Figure 4.9: Two-dimensional histograms of the $y_{fp} - \phi_{fp}$ plane before and after the transformation due to Eq. (4.6).

the homogeneity of background events in the $\phi_c - y_c$ plane. By adding(subtracting) a constant to(from) y_{fp}, two sets of artificially displaced data were created without changing ϕ_c as illustrated in Fig. 4.10(b) and (c). These were analyzed in the same manner including all software gates as applied for the unshifted data. The optimum value of the displacement depends on the excitation energy. A criterion for this method is the independence of the result from the shift direction. The background spectrum is then obtained by taking the average of the two shifted data sets. This procedure leads to the dashed red curve labeled b (for background events) in

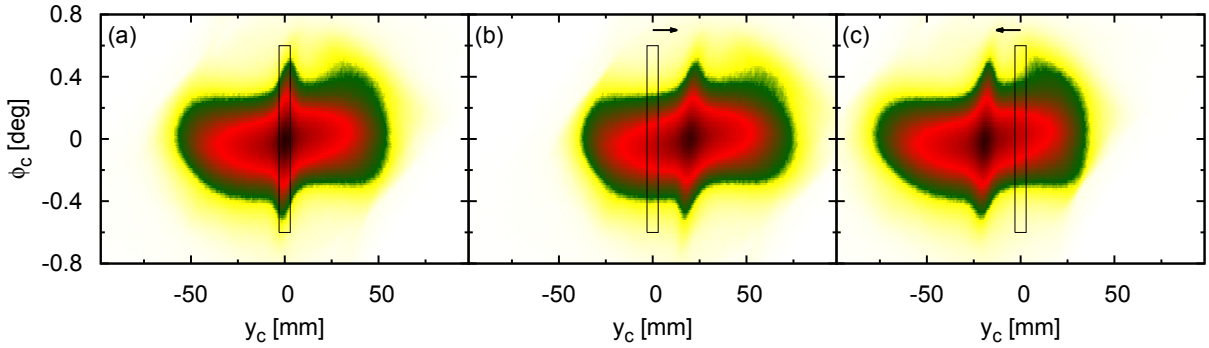

Figure 4.10: Extended method of background subtraction with the transformation due to Eq. (4.7). The black boxes illustrate the selected regions for true plus background as well as background events. The artificially shifted data sets are evoked by shifting along the arrows.

the top part of Fig. 4.11. The black curve shows the excitation energy spectrum for true plus background (t+b) events. The background-subtracted excitation energy spectrum is depicted in the bottom part of Fig. 4.11.

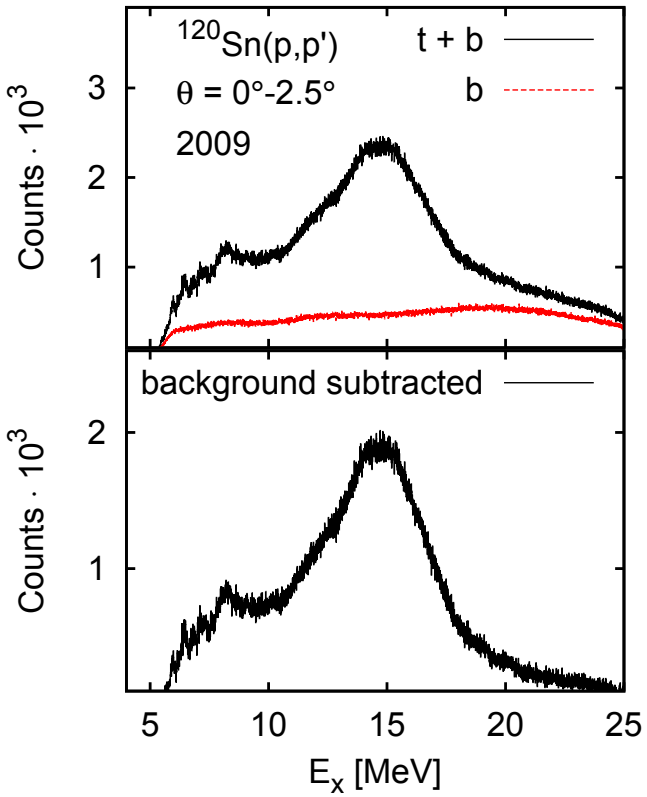

Figure 4.11: In the top part the excitation energy spectrum at $E_p = 295\,\mathrm{MeV}$ containing true plus background (t+b) events and the background (b) events are shown for ^{120}Sn. Taking the average of the two shifted data sets in Fig. 4.10 leads to the dashed red curve for background events. In the bottom part the background-subtracted spectrum is plotted.

4.6 Beam polarization determination

The beam polarization was measured by two sets of beam line polarimeters as described in Sec. 3.4. In order to derive beam polarization components $p_{N(S)}$, Eq. (3.1) can be rewritten with the assumption that $p^{\uparrow} = -p^{\downarrow}$ to

$$p_{N(S)} = \frac{1}{A_y^{BLP}} \frac{1 - X_{N(S)}}{1 + X_{N(S)}} \tag{4.8}$$

with

$$X_{N(S)} = \sqrt{\frac{N^{\uparrow}_{L(D)} N^{\downarrow}_{R(U)}}{N^{\downarrow}_{L(D)} N^{\uparrow}_{R(U)}}}. \tag{4.9}$$

The third component of the beam polarization vector at the target is obtained by combining the polarization values measured by BLP1 ($p_N^{(1)}$, $p_S^{(1)}$) and BLP2 ($p_N^{(2)}$, $p_S^{(2)}$) through the relations

$$p_N = p_N^{(1)} = p_N^{(2)}, \tag{4.10}$$

$$p_S = p_S^{(1)}, \tag{4.11}$$

$$p_L = \frac{p_S^{(1)} \cos\theta - p_S^{(2)}}{\sin\theta} \tag{4.12}$$

where θ denotes the spin precession angle in the deflecting magnet between the two BLPs given by

$$\theta = \gamma \cdot \left(\frac{g}{2} - 1\right) \cdot \theta_{BLP}\,. \tag{4.13}$$

Here, γ denotes the proton Lorentz factor, g is Lande's g-factor of the proton and θ_{BLP} stands for the bending angle of the beam. On average beam polarization values $p_S = -0.677$ and $p_L = 0.179$ were obtained during the measurements on ^{120}Sn in 2009.

4.7 Polarization analysis

The polarization transfer coefficients D_{SS} and D_{LL} at 0° can be determined by combinig information on the beam polarization from the BLPs and the polarization of the scattered protons in the Focal Plane Polarimeter

$$p_S''^{t} = \cos(\theta_p) D_{SS} p_S + \sin(\theta_p) D_{LL} p_L\,, \tag{4.14}$$

$$p_S''^{b} = \cos(\theta_p) p_S + \sin(\theta_p) p_L\,.$$

Here, $p_S''^{t(b)}$ stands for the sideway polarization component of protons after secondary scattering at the carbon slab in the FPP system for true(background) events, while p_S and p_L denote the sideway and longitudinal beam polarization. θ_p is the spin precession angle in the Grand Raiden spectrometer determined by

$$\theta_p = \gamma \cdot \left(\frac{g}{2} - 1\right) \cdot \theta_b\,. \tag{4.15}$$

Here, γ denotes the proton Lorentz factor, g is Lande′s g-factor and θ_b stands for the bending angle of the beam ($\theta_b = 162°$ for the D_{SS} and 180° for the D_{LL} measurement, respectively). For background events the assumption is made that they do not contribute to the depolarization. Thus, D_{SS} and D_{LL} are equal to unity for background events. Two different ways of polarization analysis with the FPP system are introduced in the following sections.

4.7.1 Sector method

For the sector method [14] the scattering angles of secondary scattered protons are chosen for the region of interest, U and D, as depicted in Fig. 4.12 by

$$\theta_{min} \leq \theta_{fpp} \leq \theta_{max}\,, \tag{4.16}$$

$$90° - \phi_0 \leq \mid \phi_{fpp} \mid \leq 90° + \phi_0\,. \tag{4.17}$$

The sideway component of the proton polarization is determined from the U-D scattering asym-

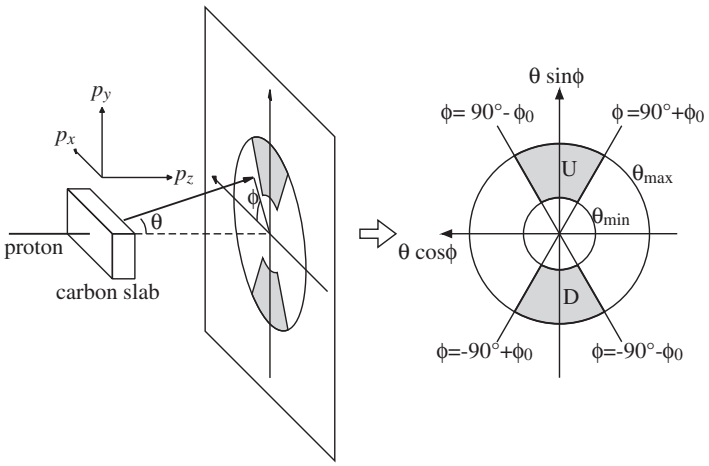

Figure 4.12: Definition of the coordinate system of secondary scattered protons at the carbon slab in the FPP. The hatched regions denote the scattering angle regimes of interest labeled by U and D.

metry

$$p_S'' = \frac{1}{\left\langle A_y \right\rangle^{fpp}} \frac{1-\alpha}{1+\alpha} \tag{4.18}$$

with the effective analyzing power of the FPP system $\left\langle A_y \right\rangle^{fpp}$ and

$$\alpha = \sqrt{\frac{N_U^{\uparrow} \cdot N_D^{\downarrow}}{N_D^{\uparrow} \cdot N_U^{\downarrow}}}, \tag{4.19}$$

where N_D and N_U denote the number of events in region U and D. The labels $\uparrow$ and $\downarrow$ stand for the beam spin orientation. The effective analyzing power $\left\langle A_y \right\rangle^{fpp}$ is determined by evaluation of a faint beam measurement.

4.7.2 Estimator method

The estimator method, which allows close to maximum use of the data, is based on an unbiased effective estimator [49]

$$\hat{\varepsilon} = \begin{pmatrix} \hat{\varepsilon}_n \\ \hat{\varepsilon}_s \end{pmatrix}, \tag{4.20}$$

which is defined as

$$\hat{\varepsilon} = \mathbf{F^{-1}B}. \tag{4.21}$$

Here,

$$\mathbf{B} = \begin{pmatrix} \sum_N \cos\phi_{fpp} \\ \sum_N \sin\phi_{fpp} \end{pmatrix} \text{ and} \tag{4.22}$$

$$\mathbf{F} = \begin{pmatrix} \sum_N \cos^2\phi_{fpp} & \sum_N \sin\phi_{fpp}\cos\phi_{fpp} \\ \sum_N \sin\phi_{fpp}\cos\phi_{fpp} & \sum_N \sin^2\phi_{fpp} \end{pmatrix}, \tag{4.23}$$

the sums $\sum_N$ are taken over all events. Statistical uncertainties are calculated from the covariant matrix

$$V(\hat{\varepsilon}) = \mathbf{F^{-1}}. \tag{4.24}$$

Taking into account the symmetry of the system when the beam spin orientation is flipped, estimators can be written as

$$\hat{\varepsilon}_N \simeq \varepsilon_N = p_N'' \left\langle A_y \right\rangle^{fpp}, \tag{4.25}$$

$$\hat{\varepsilon}_S \simeq \varepsilon_S = -p_S'' \left\langle A_y \right\rangle^{fpp} \tag{4.26}$$

with the effective analyzing power of the FPP system $\left\langle A_y \right\rangle^{fpp}$. The sideway estimators for true, background and true plus background events are defined as

$$\begin{aligned} \varepsilon_S^t &= -p_S''^t \left\langle A_y \right\rangle^{fpp}, \\ \varepsilon_S^b &= -p_S''^b \left\langle A_y \right\rangle^{fpp}, \\ \varepsilon_S^{t+b} &= \frac{N_t \varepsilon_S^t + N_b \varepsilon_S^b}{N_t + N_b} \end{aligned} \tag{4.27}$$

where N_t denotes the number of signal and N_b the number of noise events, ε_S^{t+b} is the measured asymmetry and ε_S^b is determined by the background asymmetry in the FPP.
The optimum value for the gate in the y_c histogram is specified by the following procedure: The signal-to-noise ratio N_t/N_b is determined with good statistical accuracy during the experiment. Thus, the figure of merit (FOM) can be calculated by

$$FOM = \sqrt{N_t} \frac{N_t}{N_t + N_b}. \tag{4.28}$$

It has a maximum at $1.2 - 2.0\sigma$ for ratios $N_t/N_b = 0.2 - 10$ in the y_c histogram. Thus, a value of $\pm 1.3\sigma$ corresponding to ± 3 mm on the y_c-axis was chosen for the y_c gate in the polarization analysis. Combining Eqs. (4.14) and (4.27) leads to

$$\frac{N_t + N_b}{N_t} \frac{\varepsilon_S^{t+b}}{\varepsilon_S^b} - \frac{N_b}{N_t} = \frac{D_{SS} + \frac{p_L}{p_S} \tan\theta_p D_{LL}}{1 + \frac{p_L}{p_S} \tan\theta_p} \equiv \frac{D_{SS} + c_S D_{LL}}{1 + c_S} \equiv D_{SS}^{mix} \tag{4.29}$$

$$= \frac{D_{LL} + \frac{p_S}{p_L} \tan^{-1}\theta_p D_{SS}}{1 + \frac{p_S}{p_L} \tan^{-1}\theta_p} \equiv \frac{D_{LL} + c_L D_{SS}}{1 + c_L} \equiv D_{LL}^{mix}. \tag{4.30}$$

By writing D_{SS}^{mix} and D_{LL}^{mix} equations in matrix representation

$$\begin{pmatrix} (1+c_S) D_{SS}^{mix} \\ (1+c_L) D_{LL}^{mix} \end{pmatrix} = \begin{pmatrix} 1 & c_S \\ c_L & 1 \end{pmatrix} \begin{pmatrix} D_{SS} \\ D_{LL} \end{pmatrix} \tag{4.31}$$

and inverting this matrix, D_{SS} and D_{LL} can be determined by the following relation

$$\begin{pmatrix} D_{SS} \\ D_{LL} \end{pmatrix} = \frac{1}{1 - c_S c_L} \begin{pmatrix} 1 & -c_S \\ -c_L & 1 \end{pmatrix} \begin{pmatrix} (1+c_S) D_{SS}^{mix} \\ (1+c_L) D_{LL}^{mix} \end{pmatrix}. \tag{4.32}$$

5 Results

5.1 Extraction of PTC for transitions in ^{12}C with different methods

An excitation energy spectrum of the $^{12}C(\vec{p},\vec{p}')$ reaction at 0° containing true and background events is shown in Fig. 5.1. The spectrum is based on the summation of two data runs recorded during 2008 data taking. The excitation energy ranges from 3.5 MeV to 23.5 MeV. The 0^+, $T = 0$ state at 7.65 MeV, the 1^+, $T = 0$ state at 12.71 MeV as well as the 1^+, $T = 1$ state at 15.1 MeV are clearly observed. The polarization transfer coeffcients D_{SS} and D_{LL} as well as

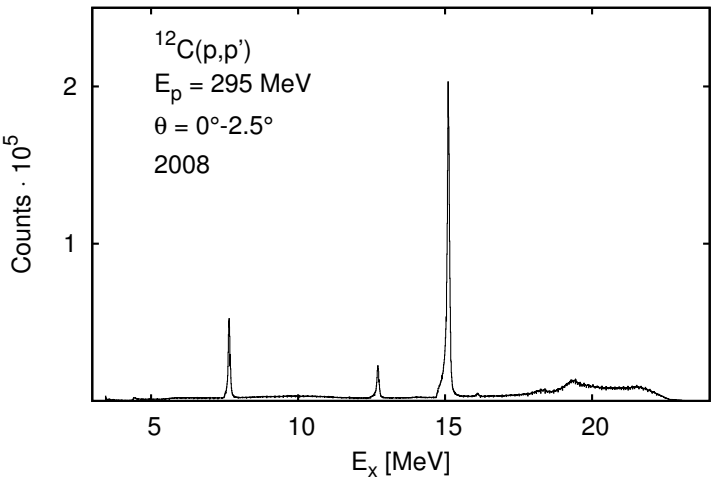

Figure 5.1: Excitation energy spectrum for ^{12}C at $E_p = 295$ MeV without background subtraction.

the total spin transfer where determined for the transition to these discrete states. Data sets from 2008 and 2009, each consisting of two runs, were combined and evaluated utilizing the sector as well as the estimator method. The results are illustrated in Fig. 5.2 comparing the actual results at 295 MeV to values extracted from a previous experiment at 392 MeV [17]. Note that the error bars only include statistical uncertainties. Furthermore, it has to be taken into account that the evaluation of the 2009 data set is based on fit parameter sets from a previous experiment. The scattering angle calibration, the correction of higher-order aberrations and the background subtraction for the 2009 measurement, described in Sec. 4, has been performed at a later date. However, the results for the total spin transfer Σ are in good agreement. The results in Fig. 5.2 show that the 0^+ state is populated by a non-spinflip transition whereas the transitions to both 1^+ states posses spinflip character.

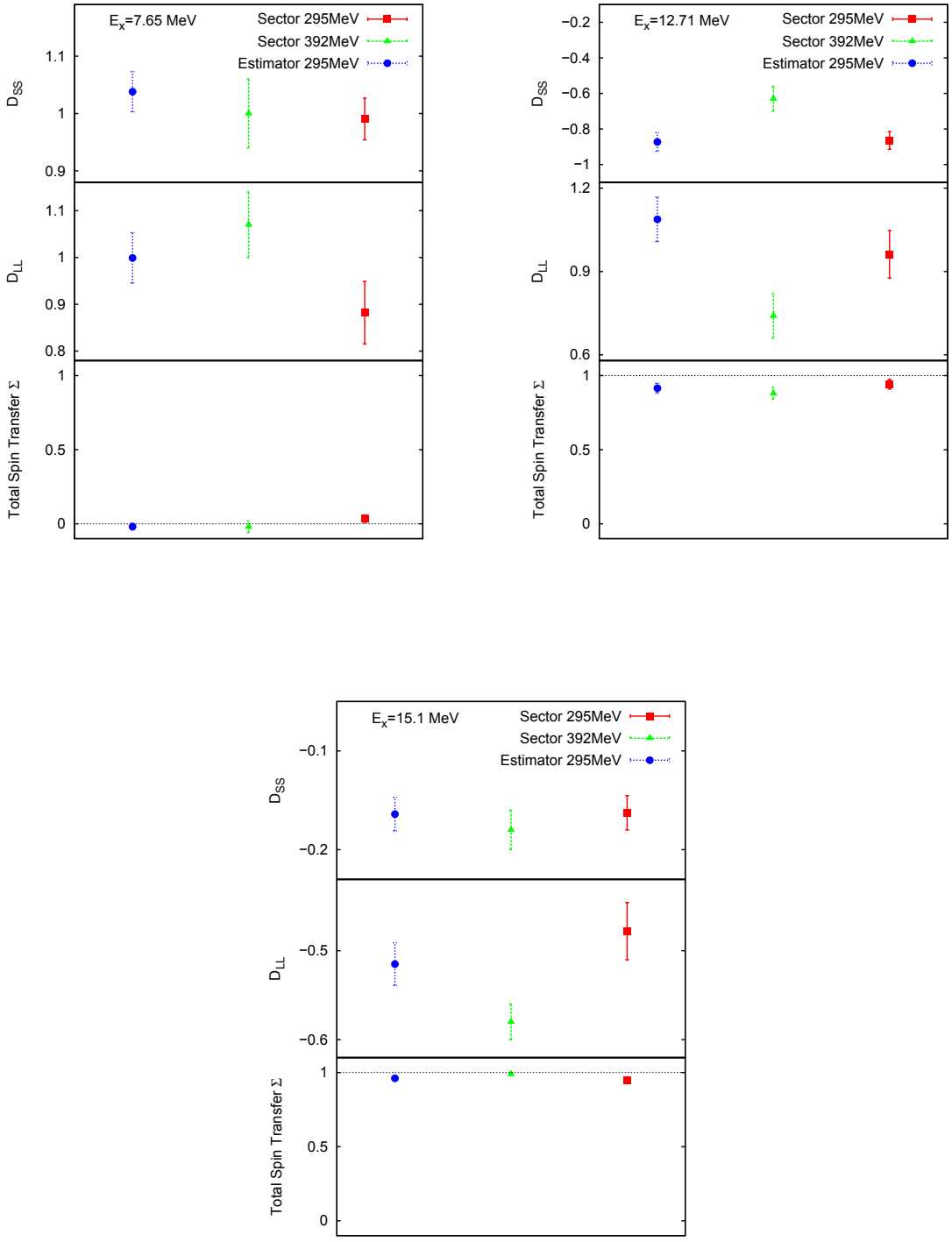

Figure 5.2: Polarization transfer coefficients D_{SS}, D_{LL} and the total spin transfer Σ for transitions to the 0^+, $T = 0$, the 1^+, $T = 0$ and the 1^+, $T = 1$ states in ^{12}C from $(\vec{p}, \vec{p}')$ measurements at incident energies of 295 and 392 MeV at 0°.

5.2 PTC for ^{208}Pb with estimator method

The PTC for ^{208}Pb have already been determined with the estimator method [30] and the deduced Σ has been published recently [19]. As a case study in this thesis the analysis was repeated independently. In the left part of Fig. 5.3 the excitation energy spectrum is shown after summing up all data runs from 2006. The background-corrected spectrum for 2006 is plotted in the left lower panel. The same procedure applied to the data in 2008 is plotted in the right part of Fig. 5.3. Figure 5.4 demonstrates the excellent agreement of the background-subtracted spectra after correction for the different overall statistics. The two upper panels of Fig. 5.5 show the polarization transfer coefficients D_{SS} and D_{LL} while the bottom panel shows the total spin transfer Σ. The main contributions to the uncertainties of D_{SS}, D_{LL} and Σ arise from the limited statistics in a secondary scattering experiment. Therefore, the error bars only include statistical uncertainties. A concentration of spinflip transitions between 7 and 9 MeV can be found. It arises from the spinflip M1 resonance. The non-spinflip character of electric dipole transitions is proven in the region of the giant dipole resonance where Σ is close to 0. For higher excitation energies the total spin transfer deviates from zero which might be explained by the spinflip part of quasielastic scattering processes [50] or by spin-dipole excitations. All in all, the results agree well within the error bars with the already performed analysis [30].

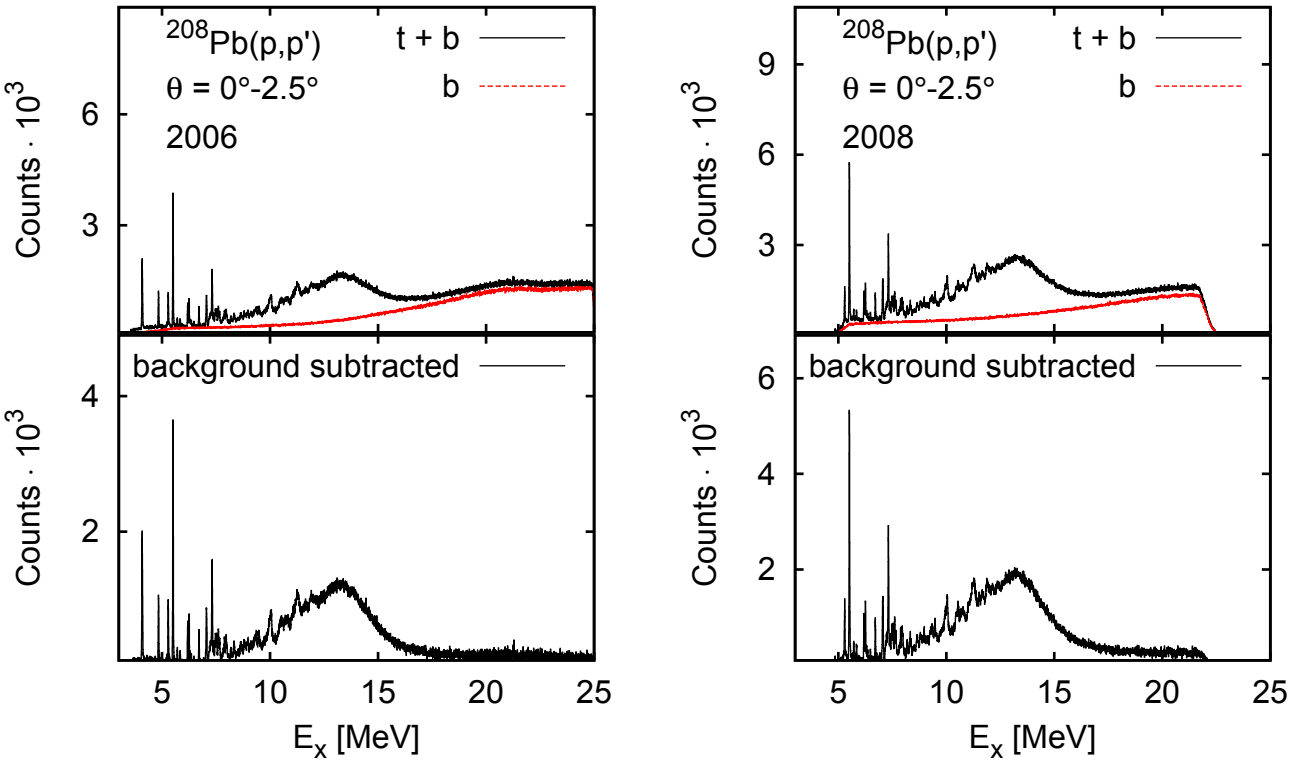

Figure 5.3: Excitation energy spectra of ^{208}Pb at $E_p = 295\,\mathrm{MeV}$ gained by adding up all runs for 2006 and 2008 measurements, respectively.

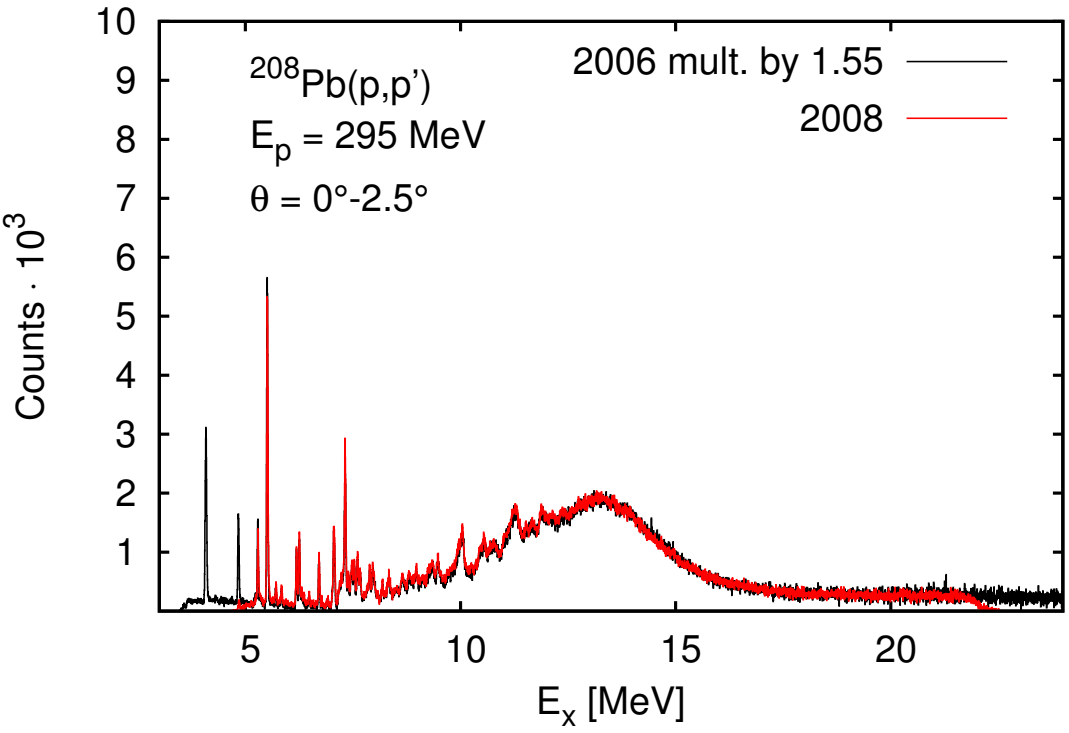

Figure 5.4: Comparison of background-subtracted excitation energy spectra of ^{208}Pb at $E_p = 295\,\mathrm{MeV}$ for the 2006 and 2008 measurements.

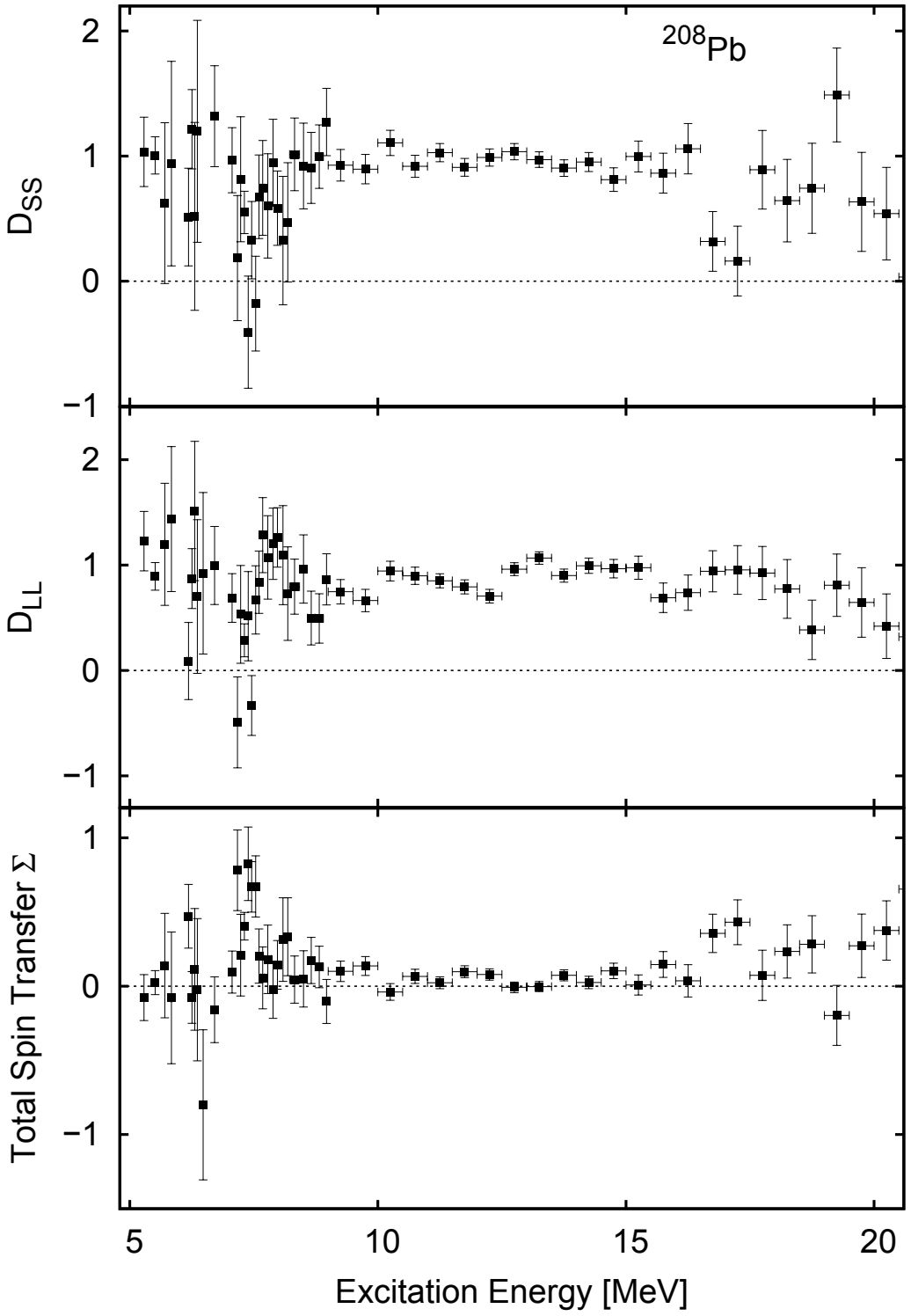

Figure 5.5: Polarization transfer coefficients D_{SS}, D_{LL} and the total spin transfer Σ for ^{208}Pb.

5.3 PTC for ^{120}Sn with estimator method

The polarization transfer coefficients for ^{120}Sn are also evaluated utilizing the estimator method. Figure 5.6 depicts the summarized spectra for the measurements in 2008 and 2009, respectively. However, after overlaying both spectra and normalizing them to the maximum of the giant dipole resonance deviations are observed as illustrated in Fig. 5.7. The measured spectrum for 2009 contains larger statistics in an excitation energy range from 7.5 to 15 MeV, whereas the tail of the GDR at higher excitation energies is more pronounced in the 2008 spectrum. This behaviour may result from an inconsistent background subtraction. A comparison to measured photoabsorption cross sections [51] may clarify this problem. The resulting PTC D_{SS} and D_{LL} and the total spin transfer Σ are illustrated for ^{120}Sn in Fig. 5.8. Note that the error bars only include statistical uncertainties. The total spin tranfer Σ indicates in an excitation energy range from 6 to 12 MeV spinflip contributions to the cross section. In the excitation energy range from 12 to 18 MeV Σ is close to zero demonstrating the non-spinflip character of the GDR. Deviations of Σ from zero for higher excitation energies may again result from the spinflip part of quasielastic scattering or spin-dipole excitations.

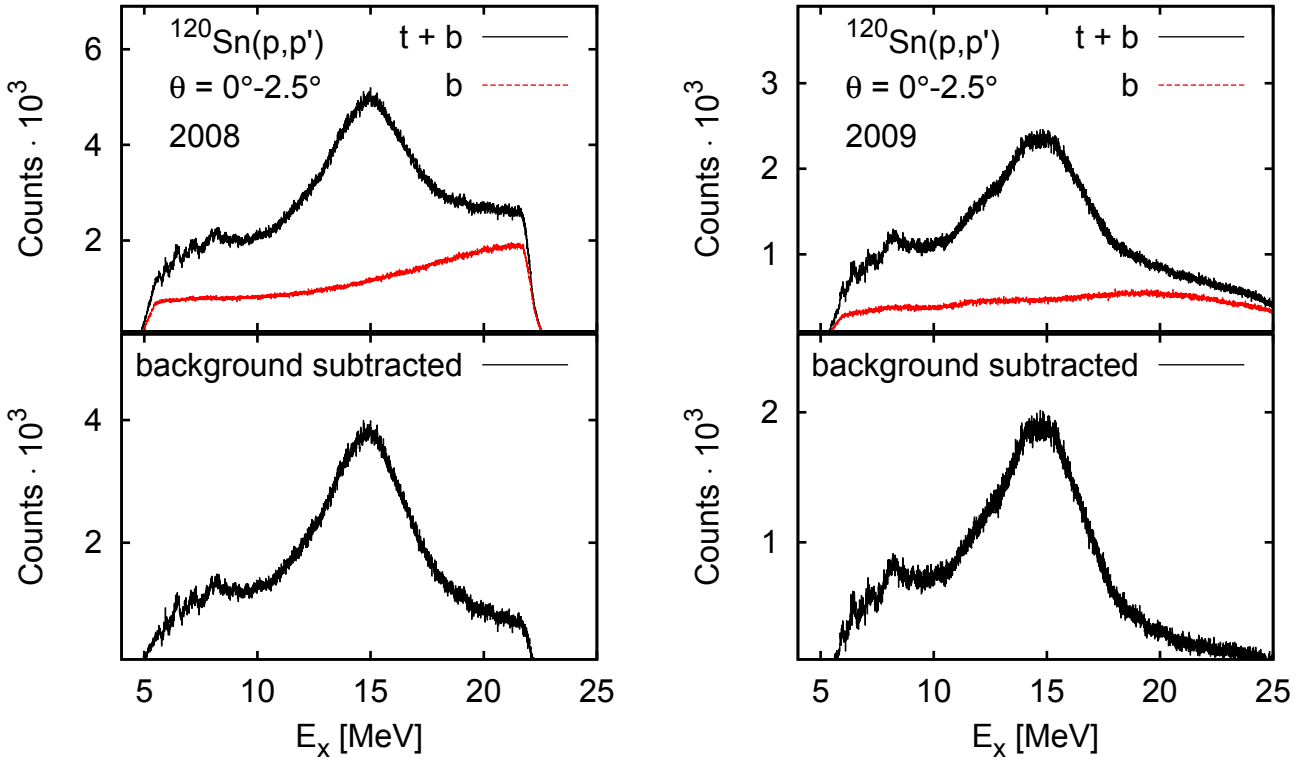

Figure 5.6: Excitation energy spectra of ^{120}Sn at $E_p = 295$ MeV gained by adding up all runs for 2008 and 2009 measurements, respectively.

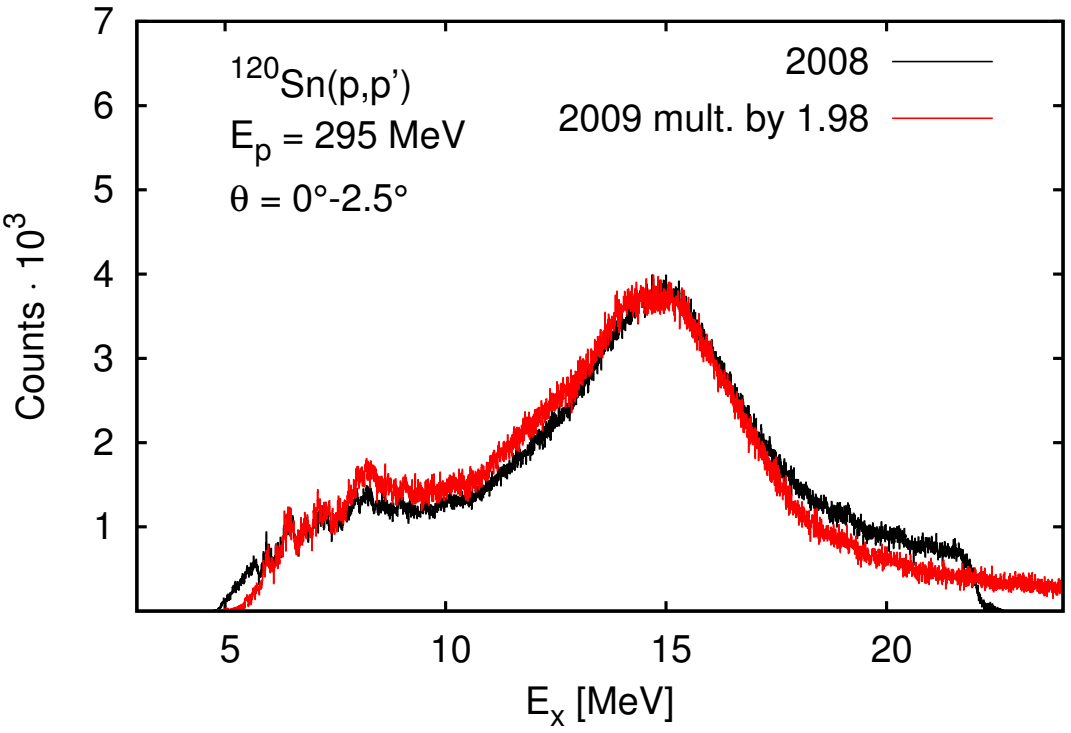

Figure 5.7: Comparison of background-subtracted excitation energy spectra of ^{120}Sn at $E_p = 295\,\mathrm{MeV}$ for the 2008 and 2009 measurements.

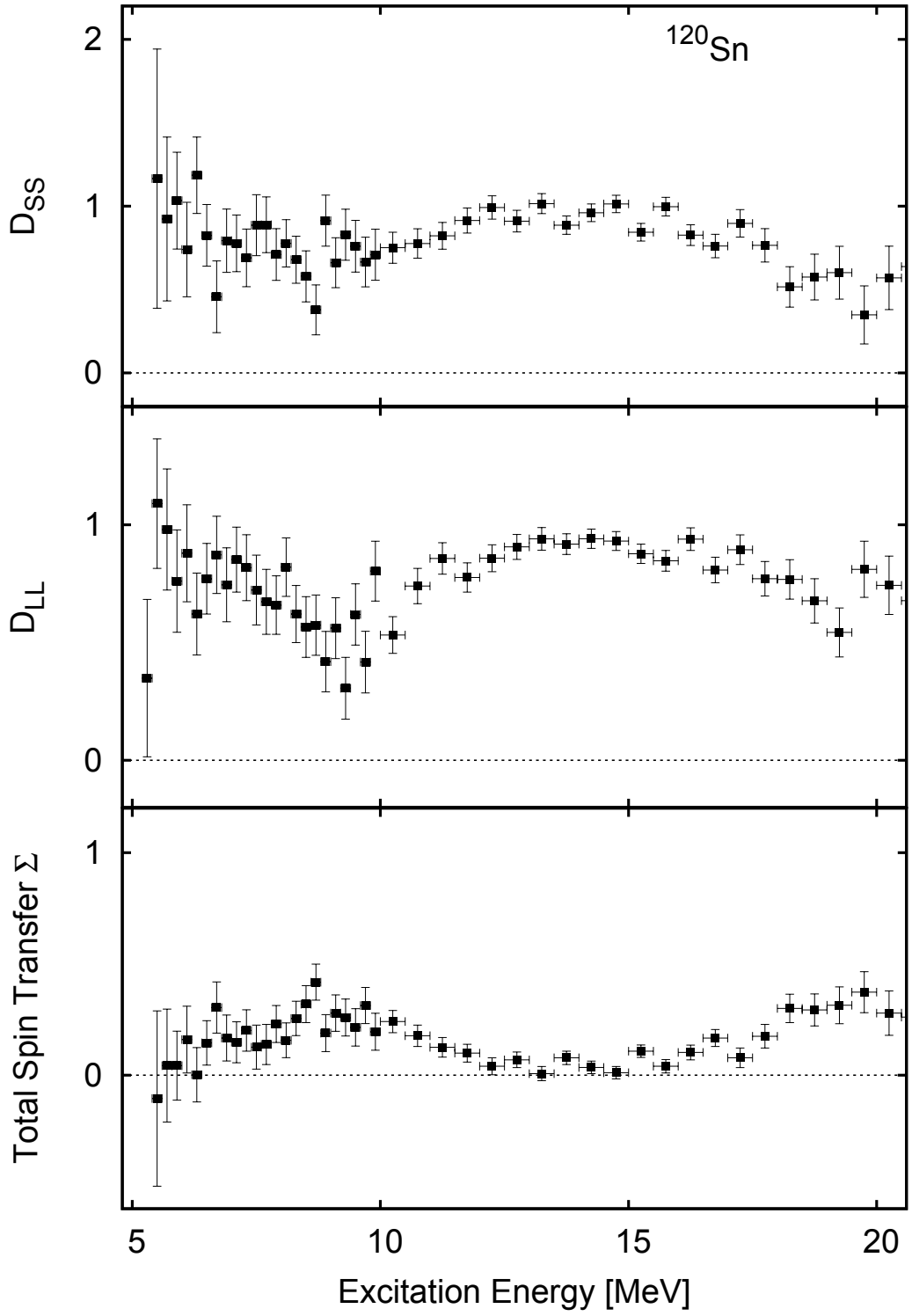

Figure 5.8: Polarization transfer coefficients D_{SS}, D_{LL} and the total spin transfer Σ for ^{120}Sn.

6 Summary and outlook

In this thesis polarization transfer coefficients have been extracted for different nuclei measured with high-resolution polarized proton scattering at 0°. Proton scattering under forward angles including 0° at the intermediate energy region of a few hundred MeV forms a new experimental tool with the unique opportunity to study the pygmy dipole resonance as well as the isovector giant dipole resonance simultaneously. Furthermore, spinflip M1 transitions can be probed. The separation of E1 and spin-M1 contributions to the cross sections can be achieved with a model-independent technique based on the measurement of PTC.

The evaluation of polarization transfer coefficients for ^{12}C as a reference case applying different extraction methods is in very good agreement with an already performed analysis [29]. For ^{208}Pb, the separation of E1 and spin-M1 transitions by PTC reproduces the results gained with a multipole decomposition analysis (MDA) based on the cross section angular distributions [30]. In case of ^{120}Sn, the total spin transfer Σ is the first approach to separate spinflip and non-spinflip transitions. By performing a MDA the results gained by PTC can be checked.

The next step in the analysis of the ^{120}Sn results is the determination of the cross section and the MDA enabling the extraction of the total B(E1) strength. Thus, the centroid energy and the total strength of the PDR can be determind below and above the particle emission threshold. Theoretical predictions for the tin isotope chain differ in the centroid energy as well as in the total strength of the PDR [4]. The M1 strength of the broad bump near 8.4 MeV assigned to be of pure spinflip nature in Ref. [12], and also found in the present analysis, can be estimated when the cross sections are known.

Another evaluation of a high-resolution polarized proton scattering experiment at 0° measuring the heavy deformed nucleus ^{154}Sm performed in May 2011 is underway. This study focuses on the role of deformation on the characteristic properties of the PDR. Moreover, it tries to clarify the double-hump structure of the spin-M1 resonance whose interpretation is unclear [5].

References

[1] J. Piekarewicz, *Phys. Rev. C* 73 (2006) 044325.

[2] A. Klimkiewicz, N. Paar, P. Adrich, M. Fallot, K. Boretzky, T. Aumann, D. Cortina-Gil, U. Datta Pramanik, Th. W. Elze, H. Emling, H. Geissel, M. Hellström, K. L. Jones, J. V. Kratz, R. Kulessa, C. Nociforo, R. Palit, H. Simon, G. Surówka, K. Sümmerer, D. Vretenar, and W. Walús, (LAND Collaboration) *Phys. Rev. C* 76 (2007) 051603(R).

[3] S. Goriely, *Phys. Lett. B* 436 (1998) 10.

[4] B. Özel, J. Enders, H. Lenske, P. von Neumann-Cosel, I. Poltoratska, V.Yu. Ponomarev, A. Richter, D. Savran, and N. Tsoneva, *submitted to Phys. Lett. B* (2009).

[5] K. Heyde, P. von Neumann-Cosel, and A. Richter, *Rev. Mod. Phys.* 82 (2010) 2365.

[6] U. Kneissl, N. Pietralla, and A. Zilges, *J. Phys. G: Nucl. Part. Phys.* 32 (2006) R217.

[7] B. Özel, *Study of the $^{112,120}Sn$ (γ,γ') reaction and systematics of the pygmy dipole resonance at the Z=50 shell closure*, Ph.D. thesis, Çukurova University, Adana, Turkey (2008).

[8] G. Rusev, R. Schwengner, R. Beyer, M. Erhard, E. Grosse, A. R. Junghans, K. Kosev, C. Nair, K. D. Schilling, A. Wagner, F. Dönau, and S. Frauendorf, *Phys. Rev. C* 79 (2009) 061302.

[9] H. J. Wörtche, *Untersuchung der M1-Stärkeverteilung in den schweren deformierten Kernen ^{150}Nd, ^{154}Sm ,^{156}Gd, ^{232}Th und ^{238}U mit polarisierter und unpolarisierter Protonenstreuung*, Doctoral thesis D17, TU Darmstadt, Germany (1994).

[10] F. Hofmann, *Streuung von polarisierten und unpolarisierten Protonen an ^{58}Ni und die mikroskopische Beschreibung von Wirkungsquerschnitten und Spinflip-Observablen*, Doctoral thesis D17, TU Darmstadt, Germany (2003).

[11] F.E. Bertrand, E.E. Gross, D.J. Horen, J.R. Wu, J. Tinsley, D.K. McDaniels, L.W. Swenson, and R. Liljestrand, *Phys. Lett. B* 103 (1981) 326.

[12] C. Djalali, N. Marty, M. Morlet, A. Willis, J.C. Jourdain, N. Anantaraman, G.M. Crawley, A. Galonsky, and P. Kitching, *Nucl. Phys. A* 388 (1982) 1.

[13] H. Fujita, Y. Fujita, T. Adachi, A.D. Bacher, G.P.A. Berg, T. Black, E. Caurier, C.C. Foster, H. Fujimura, K. Hara, K. Harada, K. Hatanaka, J. Jänecke, J. Kamiya, Y. Kanzaki, K. Katori, T. Kawabata, K. Langanke, G. Martinez-Pinedo, T. Noro, D.A. Roberts, H. Sakaguchi, Y. Shimbara, T. Shinada, E.J. Stephenson, H. Ueno, T. Yamanaka, M. Yoshifuku, and M. Yosoi, *Phys. Rev. C* 75 (2007) 034310.

[14] A. Tamii, Y. Fujita, H. Matsubara, T. Adachi, J. Carter, M. Dozono, H. Fujita, K. Fujita, H. Hashimoto, K. Hatanaka, T. Itahashi, M. Itoh, T. Kawabata, K. Nakanishi, S. Ninomiya, A.B. Perez-Cerdan, L. Popescu, B. Rubio, T. Saito, H. Sakaguchi, Y. Sakemi, Y. Sasamoto, Y. Shimbara, Y. Shimizu, F.D. Smit, Y. Tameshige, M. Yosoi, and J. Zenhiro, *Nucl. Instr. Meth. A* 605 (2009) 326.

[15] R. Neveling, H. Fujita, F.D. Smit, T. Adachi, G.P.A. Berg, E.Z. Buthelezi, J. Carter, J.L. Conradie, M. Couder, R.W. Fearick, S.V. Förtsch, D.T. Fourie, Y. Fujita, J. Görres, K. Hatanaka, M. Jingo, A.M. Krumbholz, C.O. Kureba, J.P. Mira, S.H.T. Murray, P. von Neumann-Cosel, S. O'Brien, P. Papka, I. Poltoratska, A. Richter, E. Sideras-Haddad, J.A. Swartz, A. Tamii, I.T. Usman, and J.J. van Zyl, *Nucl. Instr. Meth. A* 654 (2011) 29.

[16] A. M. Heilmann, *Complete electric dipole response in ^{120}Sn: A test of the resonance character of the pygmy dipole resonance*, Master thesis, TU Darmstadt, Germany (2009).

[17] A. Tamii, H. Akimune, I. Daito, Y. Fujita, M. Fujiwara, K. Hatanaka, K. Hosono, F. Ihara, T. Inomata, T. Ishikawa, M. Itoh, M. Kawabata, T. Kawabata, M. Nakamura, T. Noro, E. Obayashi, H. Sakaguchi, H. Takeda, T. Taki, H. Toyokawa, H.P Yoshida, M. Yoshimura, and M. Yosoi, *Phys. Lett. B* 459 (1999) 61.

[18] T. Kawabata, T. Ishikawa, M. Itoh, M. Nakamura, H. Sakaguchi, H. Takeda, T. Taki, M. Uchida, Y. Yasuda, M. Yosoi, H. Akimune, K. Yamasaki, G.P.A. Berg, H. Fujimura, K. Hara, K. Hatanaka, J. Kamiya, T. Noro, E. Obayashi, T. Wakasa, H.P. Yoshida, B. A. Brown, H. Fujita, Y. Fujita, Y. Shimbara, H. Ueno, M. Fujiwara, K. Hosono, A. Tamii, and H. Toyokawa, *Phys. Rev. C* 65 (2002) 064316.

[19] A. Tamii, I. Poltoratska, P. von Neumann-Cosel, Y. Fujita, T. Adachi, C. A. Bertulani, J. Carter, M. Dozono, H. Fujita, K. Fujita, K. Hatanaka, D. Ishikawa, M. Itoh, T. Kawabata, Y. Kalmykov, A. M. Krumbholz, E. Litvinova, H. Matsubara, K. Nakanishi, R. Neveling, H. Okamura, H. J. Ong, B. Özel-Tashenov, V.Yu. Ponomarev, A. Richter, B. Rubio, H. Sakaguchi, Y. Sakemi, Y. Sasamoto, Y. Shimbara, Y. Shimizu, F. D. Smit, T. Suzuki, Y. Tameshige, J. Wambach, R. Yamada, M. Yosoi, and J. Zenihiro, *Phys. Rev. Lett.* 107 062502 (2011).

[20] RCNP Experiment E350: *Low-energy dipole modes and deformation*.

[21] D. Martin, B.Sc. thesis, TU Darmstadt, Germany, (2011).;
A. Krugmann, Doctoral thesis D17, TU Darmstadt, Germany, in preparation.

[22] C. A. Bertulani, and G. Baur, *Phys. Rep.* 163 (1988) 299.

[23] W.G. Love and M.A. Franey, *Phys. Rev. C* 24 (1981) 1073.

[24] T. Kawabata, *Polarization transfer in the ^{16}0(p,p') reaction at forward angles and structure of the spin-dipole resonance*, Ph.D. thesis, Kyoto University, Japan (2002).

[25] A.K. Kerman, H. McManus, and R.M. Thaler, *Ann. of Phys.* 8 (1959) 551.

[26] J.M. Moss, *Phys. Rev. C* 26 (1982) 727.

[27] T. Suzuki, *Prog. Theor. Phys.* 321 (2000) 859.

[28] H. Sakai, T. Wakasa, H. Okamura, T. Nonaka, T. Ohnishi, K. Yako, K. Sekiguchi, S. Fujita, Y. Satou, H. Otsu, T. Uesaka, S. Ishida, N. Sakamoto, M.B. Greenfield, and K. Hatanaka, in Proceedings of the International Symposium of New Facet of Spin Giant Resonances in Nuclei, Tokyo, Japan, 1997, edited by H. Sakai, H. Okamura, and T. Wakasa (World Scientific, Singapore 1998) p.29.

[29] A. Tamii, *Polarization transfer observables from proton inelastic scattering from ^{12}C at zero degrees*, Ph.D. thesis, Kyoto University, Japan (1999).

[30] I. Poltoratska, *Complete dipole response in ^{208}Pb from high-resolution polarized proton scattering at* 0°, Doctoral thesis D17, TU Darmstadt, Germany (2011).

[31] K. Hatanaka, K. Takahisa, H. Tamura, M. Sato, and I. Miura, *Nucl. Instr. Meth. A* 384 (1997) 575.

[32] T. Shimoda, H. Miyatake, and S. Morinobu, *Nucl. Instr. Meth. B* 70 (1992) 320.

[33] H. Sakai, H. Okamura, H. Otsu, T. Wakasa, S. Ishida, N. Sakamoto, T. Uesaka, Y. Satou, S. Fujita, and K. Hatanaka, *Nucl. Instr. Meth. A* 369 (1996) 120.

[34] T. Wakasa, K. Hatanaka, Y. Fujita, G.P.A. Berg, H. Fujimura, H. Fujita, M. Itoh, J. Kamiya, T. Kawabata, K. Nagayama, T. Noro, H. Sakaguchi, Y. Shimbara, H. Takeda, K. Tamura, H. Ueno, M. Uchida, M. Uraki, and M. Yosoi, *Nucl. Instr. Meth. A* 482 (2002) 79.

[35] N. Matsuoka, K. Hatanaka, S. Morinobu, T. Noro, A. Okihana, and K. Sagara, *RCNP Annual Report* (1991) 186.

[36] M. Fujiwara, H. Akimune, I. Daito, H. Fujimura, Y. Fujita, K. Hatanaka, H. Ikegami, I. Katayama, K. Nagayama, N. Matsuoka, S. Morinobu, T. Noro, M. Yoshimura, K. Sakaguchi, Y. Sakemi, A. Tamii, and M. Yosoi, *Nucl. Instr. Meth. A* 422 (1999) 484.

[37] T. Noro, Y. Mizuno, H. Togawa, S. Hirata, N. Matsuoka, O. Kamigaito, F. Hiei, Y. Sakemi, H. Akimune, and T. Takahashi, *RCNP Annual Report* (1990) 217.

[38] M. Yosoi, H. Akimune, I. Daito, H. Fujiwara, S. Hirata, T. Inomata, O. Kamigaito, M. Kawabata, T. Noro, Y. Sakemi, T. Takahashi, A. Tamii, S. Toyama, A. Yamagoshi, M. Yoshimura, and H. Sakaguchi, *AIP Conf. Proc.* 343 (1995) 157.

[39] H. Fujita, Y. Fujita, G.P.A. Berg, A.D. Bacher, C.C. Foster, K. Hara, K. Hatanaka, T. Kawabata, T. Noro, H. Sakaguchi, Y. Shimbara, T. Shinada, E.J. Stephenson, H. Ueno, and M. Yosoi, *Nucl. Instr. Meth. A* 484 (2002) 17.

[40] H. Fujita, G.P.A. Berg, Y. Fujita, K. Hatanaka, T. Noro, E.J. Stephenson, C.C. Foster, H. Sakaguchi, M. Itoh, T. Taki, K. Tamura, and H. Ueno, *Nucl. Instr. Meth. A* 469 (2001) 55.

[41] A. Tamii, *priv. communication* (2011).

[42] `http://cern.ch/paw/`, `http://cern.ch/cernlib/`.

[43] RCNP Experiment E316: *Complete electric dipole response in ^{120}Sn: a test of the resonance character of the pygmy dipole resonance*.

[44] M. Galassi, J. Davies, J. Theiler, B. Gough, B. Jungman, M. Booth, and F. Rossi, *GNU Scientific Library Reference Manual, 2nd ed.* (Network Theory Ltd., Bristol, 2003); `http://www.gnu.org/software/gsl/`.

[45] H. Matsubara, *Study of M1 Quenching in ^{28}Si by a (p,p') Measurement at zero-degrees*, M.Sc. thesis, Osaka University, Japan (2006).

[46] Computer program KINMAT, iThemba Laboratory for Accelerator Based Sciences, Faure, South Africa, unpublished.

[47] N. Braun, Computer program HDTV, `https://www.ikp.uni-koeln.de/projects/hdtv/trac/`.

[48] Computer program Wolfram Mathematica 7, Version 7.0.1.0.

[49] D. Besset, B. Favier, L.G. Greeniaus, R. Hess, C. Lechanoine, D. Rapin, and D.W. Werren, *Nucl. Instr. Meth.* 166 (1979) 515.

[50] F.T. Baker, L. Bimbot, C. Djalali, C. Glashausser, H. Lenske, W.G. Love, M. Morlet, E. Tomasi-Gustafsson, J. van der Wiele, J. Wambach, and A. Willis, *Phys. Rep.* 289 (1997) 235.

[51] B. L. Berman, and S. C. Fultz, *Rev. Mod. Phys.* 47 (1975) 713.

Erklärung zur Eigenständigkeit

Hiermit versichere ich, Johannes Simonis, die vorliegende Bachelor-Thesis ohne Hilfe Dritter und nur mit den angegebenen Quellen und Hilfsmitteln angefertigt zu haben. Alle Stellen, die aus Quellen entnommen wurden, sind als solche kenntlich gemacht worden. Diese Arbeit hat in gleicher oder ähnlicher Form noch keiner Prüfungsbehörde vorgelegen.

Darmstadt, den 25. Oktober 2011

Johannes Simonis